Electronic Supplementary Material (ESI) for Journal of Materials Chemistry C.

Supplementary information

Tunable electroactive oligothiophene-naphthalimide semiconductors via end-capped engineering: Cumulative effects beyond the linker

Matías J. Alonso-Navarro,[a,b,†] Alexandra Harbuzaru,[c,†] Raúl González-Núñez,[c] M. Mar Ramos,[b] José L. Segura,[a*] Rocío Ponce Ortiz.[c*]

[a] *Department of Organic Chemistry, Complutense University of Madrid, Faculty of Chemistry, Madrid 28040, Spain.*

[b] *Chemical and Environmental Technology Department. Univ. Rey Juan Carlos, Móstoles, 28933, Spain.*

[c] *Department of Physical Chemistry, University of Málaga, Málaga, 29071, Spain.*

[†]These authors contributed equally to this work.

General contents

1. General Information

All the chemicals were purchased from commercial suppliers and used without further purification. **NIA** and **1** compounds were obtained as previously described.[1, 2] ^{1}H-NMR and ^{13}C-NMR spectra were recorded on a Bruker Avance 300 MHz and AMX 500 spectrometers. Chemical shifts are reported in ppm and referenced to the residual non-deuterated solvent frequencies ($CDCl_3$: δ 7.26 ppm for ^{1}H, δ 77.0 ppm for ^{13}C, TFA-*d*: δ 11.50 ppm for ^{1}H, δ 164.2 and 116.6 ppm for ^{13}C,). UV–vis absorption spectra of the compounds in HPLC chloroform solutions at 20 ºC were recorded on a Varian Cary 50 UV–vis spectrophotometer. Mass spectra were recorded on a Bruker Reflex 2 (MALDI-TOF). FTIR spectra were carried out in a Shimadzu FTIR 8300 spectrophotometer. Cyclic voltammograms were recorded in an inert atmosphere in electrochemical workstation at a scan rate of 100 mV·s-1 at 20 ºC using tetrabutylammonium hexafluorophosphate (TBAPF6, 0.1 mol L^{-1}) as supporting electrolyte in dichloromethane. Polymer-precoated platinum electrode, platinum–wire electrode, and Ag/Ag^{+} electrode were used as working electrode, an auxiliary electrode, and reference electrode, respectively. Potentials were recorded versus Fc/Fc^{+}.

2. Synthesis of compounds and characterization

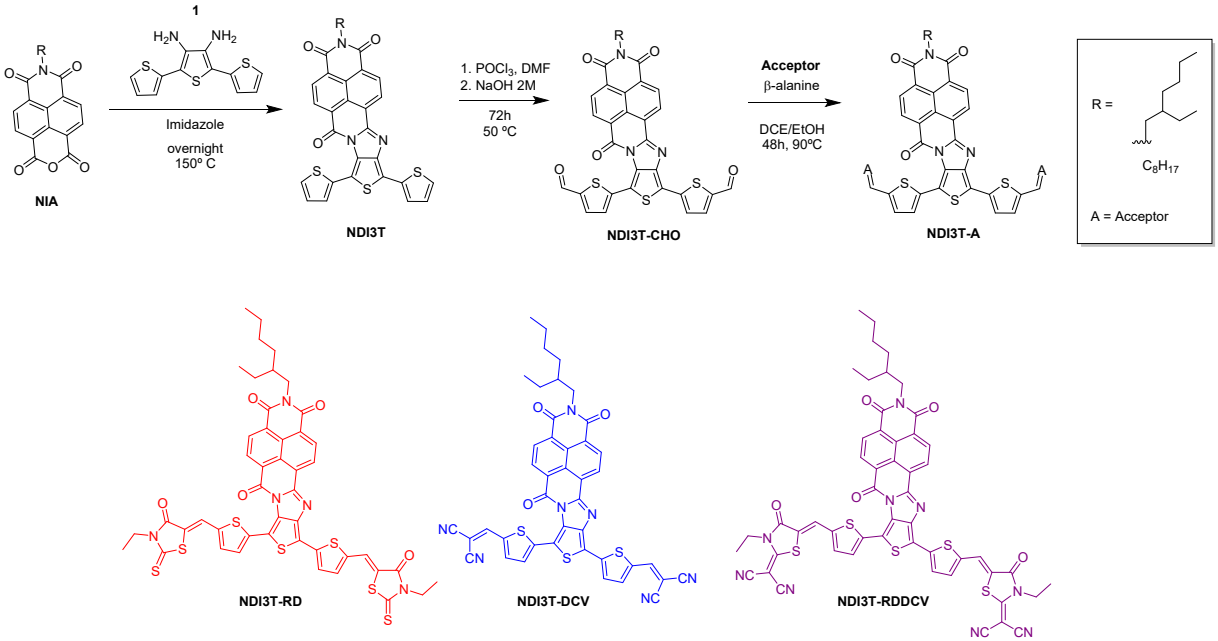

Scheme S1. Synthetic pathway for the novel A2-D-A1-D-A2 derivatives obtained in this work based on terthiophene-naphthalimide assemblies.

NDI3T: A mixture of **NIA** (339.3 mg; 0.9 mmol), **1** (226.4 mg, 0.81 mmol) and imidazole (9 g, 123 mmol) is heated at 150ºC overnight. After the reaction time is completed, the crude is cooled and then poured into 200mL of HCl 18%. The mixture is extracted five times with DCM (5x25mL) and the organic phases were mixed, dried over anhydrous $MgSO_4$, filtered and the solvent is removed under reduce pressure. The crude solid was then purified by chromatography column (silica gel flash, dichloromethane) to obtain 277 mg (55%) of a green solid.

^{1}H-NMR (300 MHz, $CDCl_3$) δ (ppm) = 8.85 (d, *J* = 7.7 Hz, 1H), 8.74 (d, *J* = 3.3 Hz, 1H), 8.71 (d, *J* = 3.3 Hz, 1H), 8.66 (d, *J* = 7.7 Hz, 1H), 7.54 – 7.49 (m, 2H), 7.38 (dd, *J* = 5.0, 3.0 Hz, 1H), 7.26 (d, *J* = 3.0 Hz, 1H), 7.20 (dd, *J* = 5.0, 3.0 Hz, 1H), 7.11 (dd, *J* = 5.0, 3.0 Hz, 1H), 4.21 – 4.05 (m, 2H), 2.00 – 1.90 (m, 1H), 1.48 – 1.26 (m, 8H), 1.00 – 0.88 (m, *J* = 15.8, 7.2 Hz, 6H).

^{13}C- NMR (75 MHz, $CDCl_3$) δ (ppm) = 163.34, 163.09, 156.81, 145.42, 143.28, 140.59, 133.52, 132.94, 131.26, 130.91, 130.78, 130.71, 128.01, 127.59, 127.13, 127.02, 126.92, 126.34, 125.45, 125.40, 124.79, 44.69, 38.18, 30.88, 28.80, 24.18, 23.25, 14.28, 10.75.

MALDI-HRMS (m/z) calc. for $C_{34}H_{27}N_3O_3S_3$: 621.1215, found (M^+): 621.1193.

FTIR (ATR, $CHCl_3$) υ (cm^{-1}) = 2958, 2924, 2854, 1707, 1666, 1463, 1376, 1338, 1297, 1263, 1241, 1071, 761, 689, 591.

m.p.: 264-265 ºC.

NDI3T-CHO: To a solution of **NDI3T** (126mg, 0,2 mmol) in 15 mL of chloroform, DMF was added in excess (1 mL) and the solution was stirred for 5min. After that, $POCl_3$ (1 mL) was added carefully and the reaction was stirred at 50 ºC for 48h. 1M NaOH (30 mL) was added, the mixture was stirred vigorously, and the phases were separated. The aqueous phase was extracted with dichloromethane and the combined organic phases were washed with water and brine and dried over $MgSO_4$. The solvent was evaporated under reduced pressure and the crude was purified by chromatography column (silica gel flash, chloroform) to provide 115 mg (83%) as greenish pure product.

^{1}H- NMR (300 MHz, $CDCl_3$) δ (ppm) = 9.99 (s, 1H), 9.95 (s, 1H), 8.97 (d, *J* = 7.6 Hz, 1H), 8.81 – 8.73 (m, 3H), 7.83 (d, *J* = 3.9 Hz, 1H), 7.76 (d, *J* = 3.9 Hz, 1H), 7.66 (d, *J* = 3.8 Hz, 1H), 7.36 (d, *J* = 3.8 Hz, 1H), 4.15 – 4.13 (m, 2H), 1.98 – 1.91 (m, 1H), 1.36 (m, 8H), 0.92 (m, 6H).

^{13}C- NMR (75 MHz, $CDCl_3$) δ (ppm) = 182.84, 182.54, 163.06, 162.86, 157.03, 155.75, 147.88, 145.95, 144.77, 143.47, 142.32, 142.17, 136.80, 135.67, 131.50, 131.29, 131.15, 130.21,

127.71, 127.57, 127.38, 126.62, 126.22, 126.10, 125.46, 125.17, 121.82.

MALDI-HRMS (m/z) calc. for $C_{36}H_{27}N_3O_5S_3$: 677.1113, found (M^+): 677.1166.

FTIR (ATR, $CHCl_3$) υ (cm^{-1}) = 2960, 2923, 2854, 1709, 1665, 1445, 1382, 1335, 1258, 1219, 1068, 827, 760, 672, 591.

m.p.: 235-236 ºC.

General procedure for the synthesis of the end-capped derivatives:[3]

To a solution of the corresponding dialdehyde derivative **NDI3T-CHO** (1eq) in 21 mL of a mixture of DCE/EtOH (5:2), **β-Alanine** (1.75eq) and the **acceptor** (3,25eq) were added, and the mixture was stirred under reflux for 48h. The solvent was removed under reduced pressure and the residue was redissolved in DCM and precipitated in MeOH.

NDI3T-RD: The solid was filtered and washed with water, MeOH and hot MeOH to obtain the product 30 mg (45 %) as a black-red material.

^{1}H- NMR (300 MHz, $CDCl_3$) δ (ppm) = 9.03 (d, *J* = 7.7 Hz, 1H), 8.87 – 8.72 (m, 3H), 7.90 (s, 1H), 7.85 (s, 1H), 7.69 (d, *J* = 4.0 Hz, 1H), 7.47 (d, *J* = 4.0 Hz, 1H), 7.40 (d, *J* = 4.0 Hz, 1H), 7.32 (d, *J* = 4.0 Hz, 1H), 4.28 – 4.09 (m, 6H), 2.01 – 1.91 (m, 1H), 1.44 – 1.24 (m, 14H), 0.93 - 0.81 (m, 6H).

^{13}C- NMR (175 MHz, $CDCl_3$) δ (ppm) = 191.73, 191.53, 191.47, 167.17, 162.96, 162.79, 157.24, 156.91, 156.28, 155.34, 150.27, 149.69, 148.76, 147.41, 144.06, 143.85, 140.65, 140.30, 139.33, 138.49, 138.06, 136.59, 135.50, 134.98, 133.97, 132.28, 131.94, 131.54, 131.16, 130.58, 129.99, 129.70, 128.14, 127.80, 127.63, 127.35, 126.81, 126.33, 126.20, 125.29, 125.04, 124.59, 121.79, 121.44, 114.01, 113.58, 113.08, 44.66, 40.05, 37.95, 31.90, 30.66, 28.59, 27.07, 23.98, 23.04, 14.09, 12.30, 10.56.

MALDI-HRMS (m/z) calc. for $C_{46}H_{37}N_5O_5S_7$: 963.0840, found (M^+): 963.049.

FTIR (ATR, $CHCl_3$) υ (cm^{-1}) = 2959, 2923, 2853, 1708, 1667, 1579, 1463, 1432, 1375, 1328, 1258, 1235, 1131, 1094, 1014, 825, 798, 760, 682, 598.

m.p..: 308-309 ºC.

NDI3T-DCV: The solid was filtered and washed with water, MeOH and hot MeOH to obtain the product 35 mg (60 %) as a black-red material.

^{1}H- NMR (300 MHz, $CDCl_3$/TFA-*d*) δ (ppm) = 8.96 (d, *J* = 7.8 Hz, 1H), 8.81 – 8.68 (m, 3H), 7.85 – 7.78 (m, 3H), 7.77 – 7.72 (m, 2H), 7.34 (d, *J* = 4.1 Hz, 1H), 4.12 – 3.97 (m, 2H), 1.96 – 1.80 (m, 1H), 1.37 – 1.19 (m, 8H), 0.90 – 0.72 (m, 6H).

MALDI-HRMS (m/z) calc. for $C_{42}H_{27}N_7O_3S_3$: 773.1337, found (M^+): 773.1325.

FTIR (ATR, $CHCl_3$) υ (cm^{-1}) = 2993, 2958, 2922, 2854, 2221, 1706, 1667, 1569, 1494, 1462, 1433, 1404, 1376, 1359, 1338, 1293, 1258, 1223, 1205, 1183, 1142, 1099, 1085, 1068, 1018, 876, 823, 811, 801, 764, 733, 720, 622, 608.

m.p.: 310-311 ºC.

NDI3T-RDDCV: The solid was filtered and washed with water, MeOH and hot MeOH to obtain the product 46 mg (61 %) as a purple powder.

^{1}H- NMR (300 MHz, $CDCl_3$/TFA-*d*) δ (ppm) = 9.03 (d, *J* = 8.1 Hz, 1H), 8.88 – 8.77 (m, 3H), 8.14 (s, 1H), 8.12 (s, 1H), 7.73 (d, *J* = 4.4 Hz, 1H), 7.56 (d, *J* = 4.4 Hz, 1H), 7.53 (d, *J* = 3.8 Hz, 1H), 7.43 (d, *J* = 4.3 Hz, 1H), 4.37 (d, *J* = 6.8 Hz, 2H), 4.21 (q, *J* = 7.1 Hz, 6H), 2.05 – 1.94 (m, 1H), 1.49 – 1.31 (m, 14H), 0.94 – 0.83 (m, 6H).

MALDI-HRMS (m/z) calc. for $C_{52}H_{37}N_9O_5S_5$: 1027,1521, found (M^+): 1027,1517.

FTIR (ATR, $CHCl_3$) υ (cm^{-1}) = 2953, 2922, 2853, 2217, 1707, 1665, 1573, 1540, 1460, 1445, 1428, 1375, 1334, 1215, 1196, 1123, 1055, 793, 763, 730.

m.p.: 314-315 ºC.

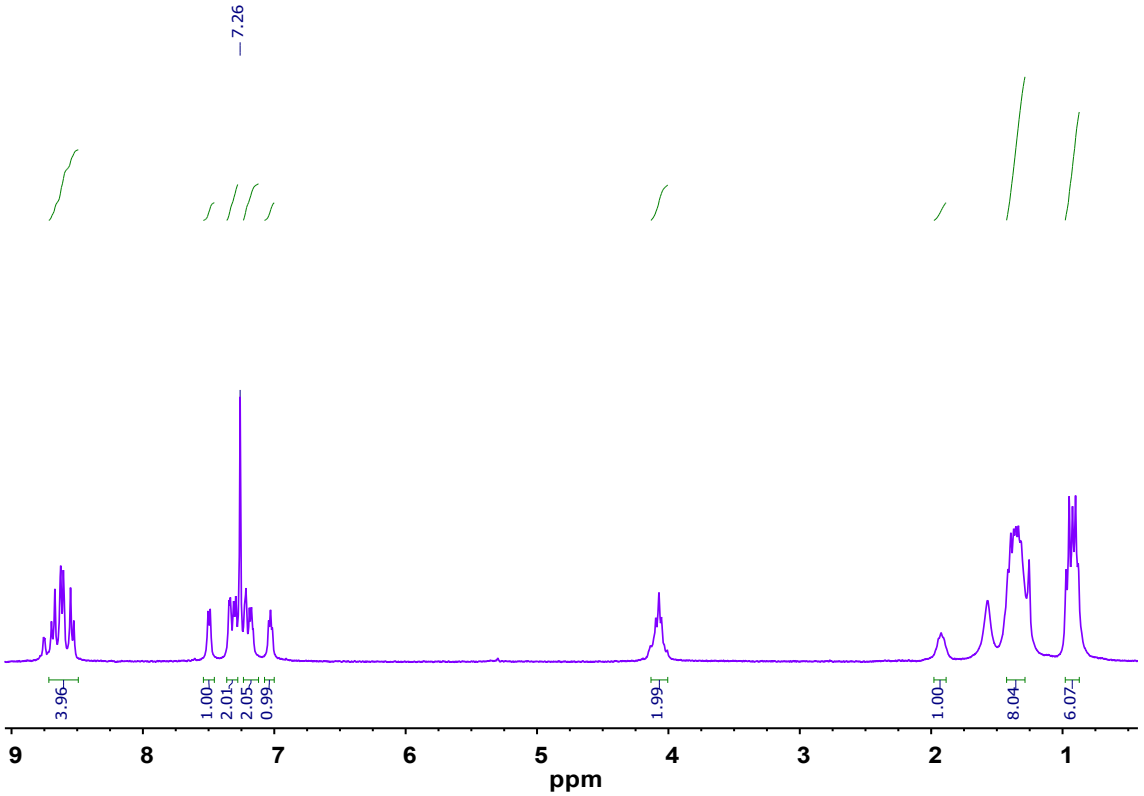

Figure S1. ^{1}H-NMR spectrum of **NDI3T** in $CDCl_3$.

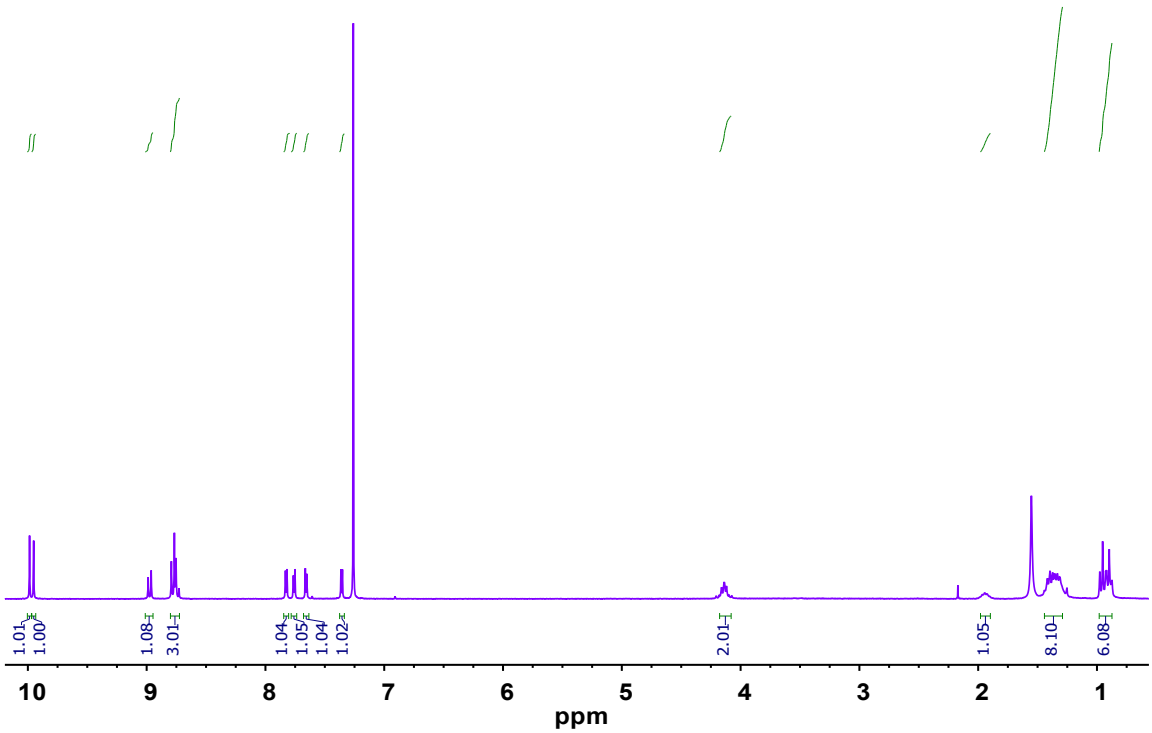

Figure S2. ^{1}H-NMR spectrum of **NDI3T-CHO** in $CDCl_3$.

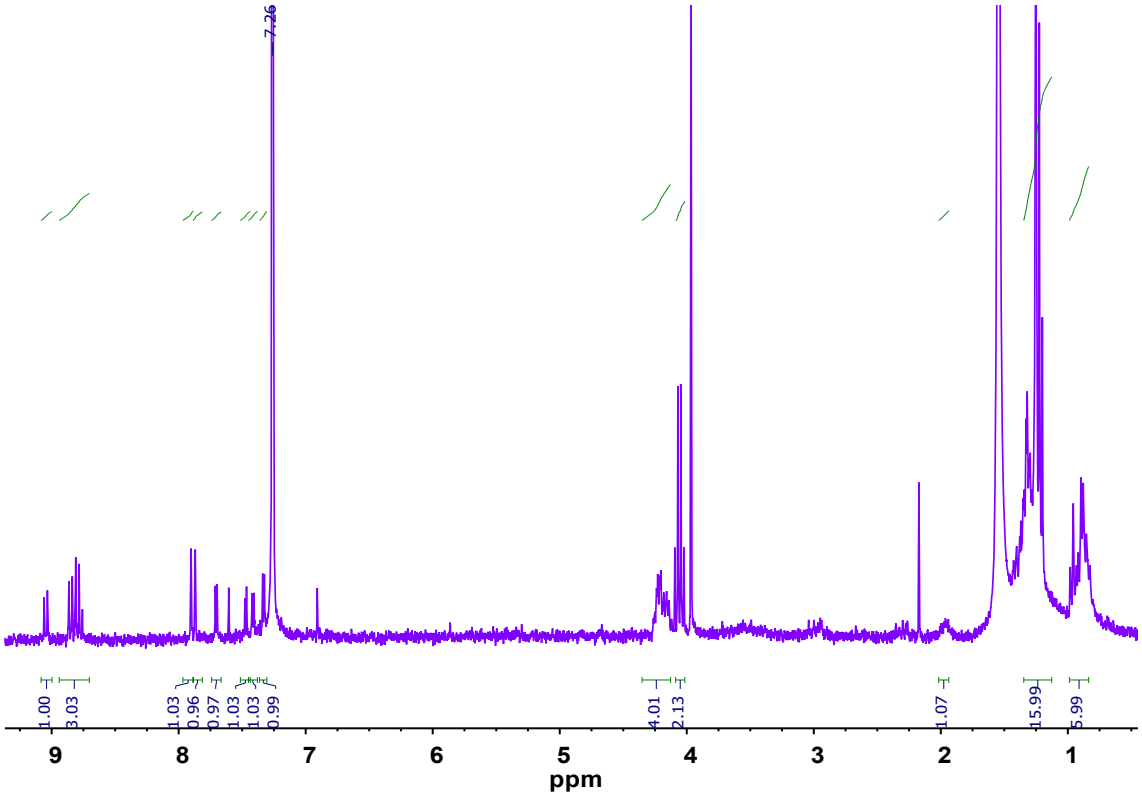

Figure S3. ^{1}H-NMR spectrum of **NDI3T-RD** in $CDCl_3$.

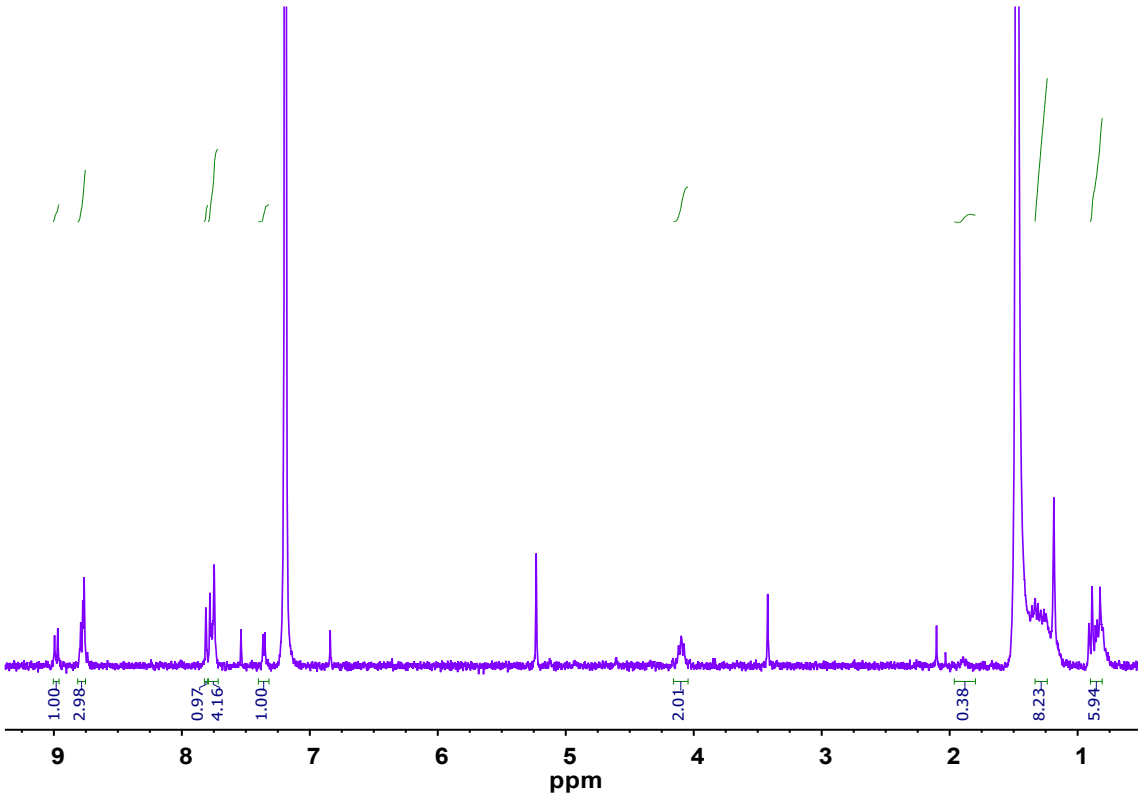

Figure S4. ^{1}H-NMR spectrum of **NDI3T-DCV** in $CDCl_3$/TFA-*d*.

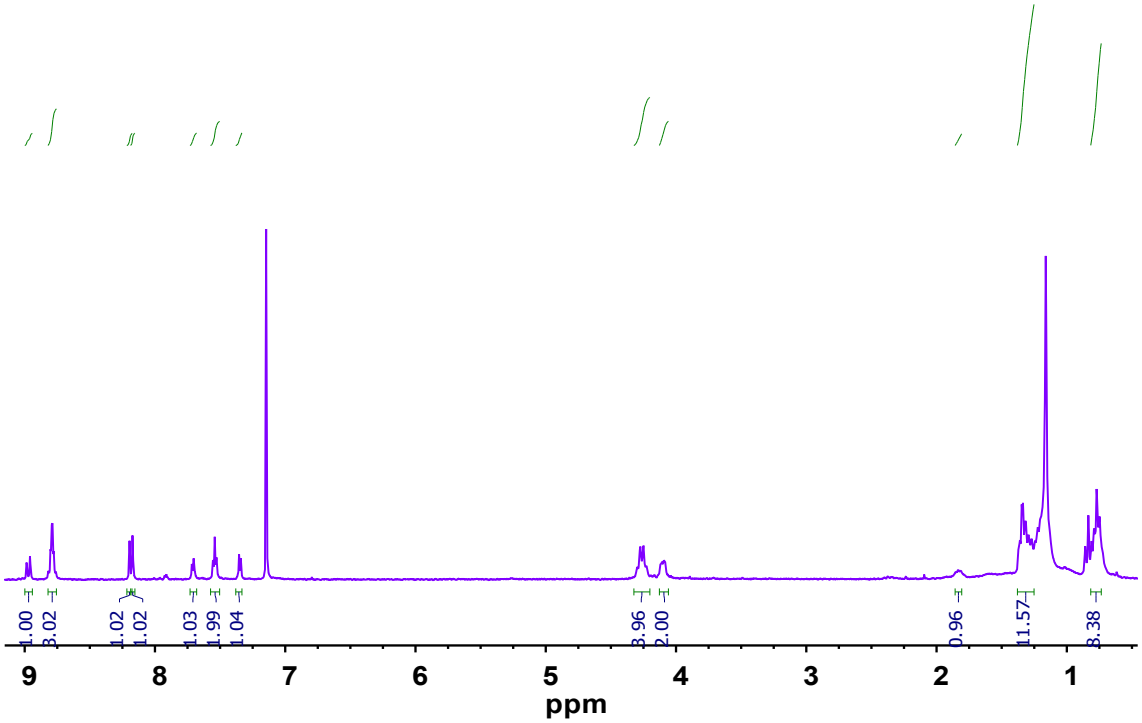

Figure S5. ^{1}H-NMR spectrum of **NDI3T-RDDCV** in $CDCl_3$/TFA-*d*.

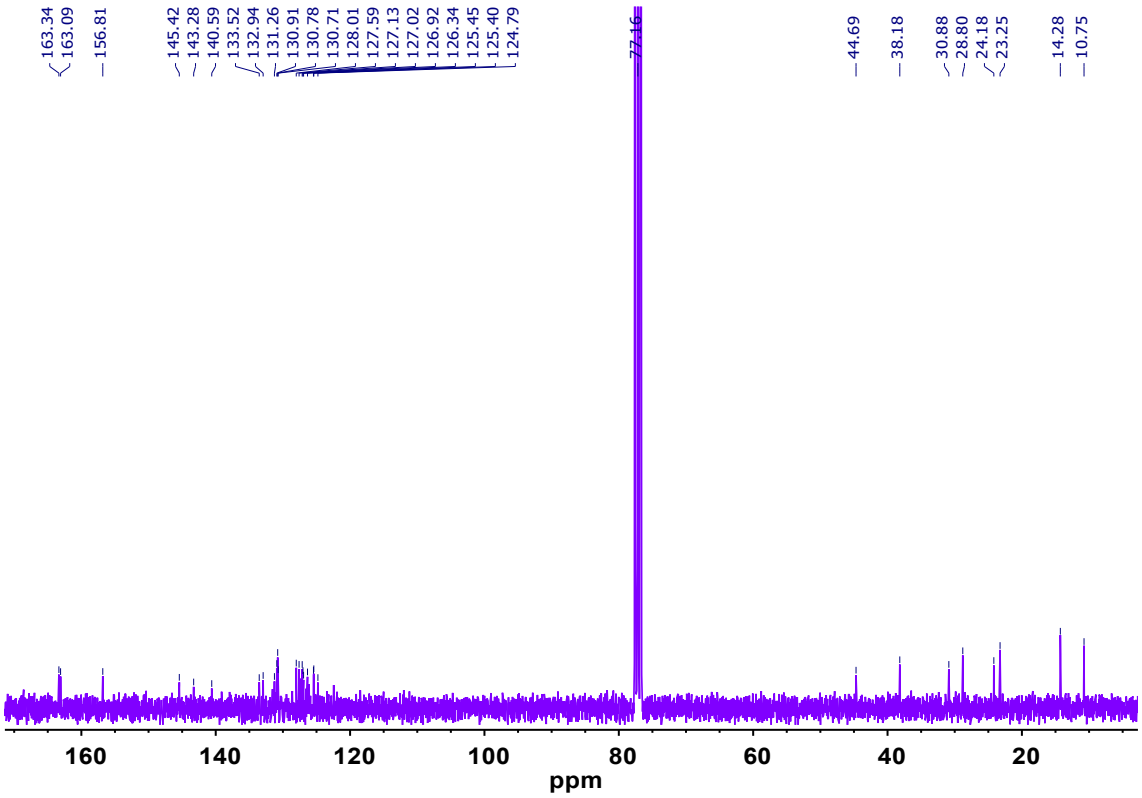

Figure S6. ^{13}C-NMR spectrum of **NDI3T** in $CDCl_3$.

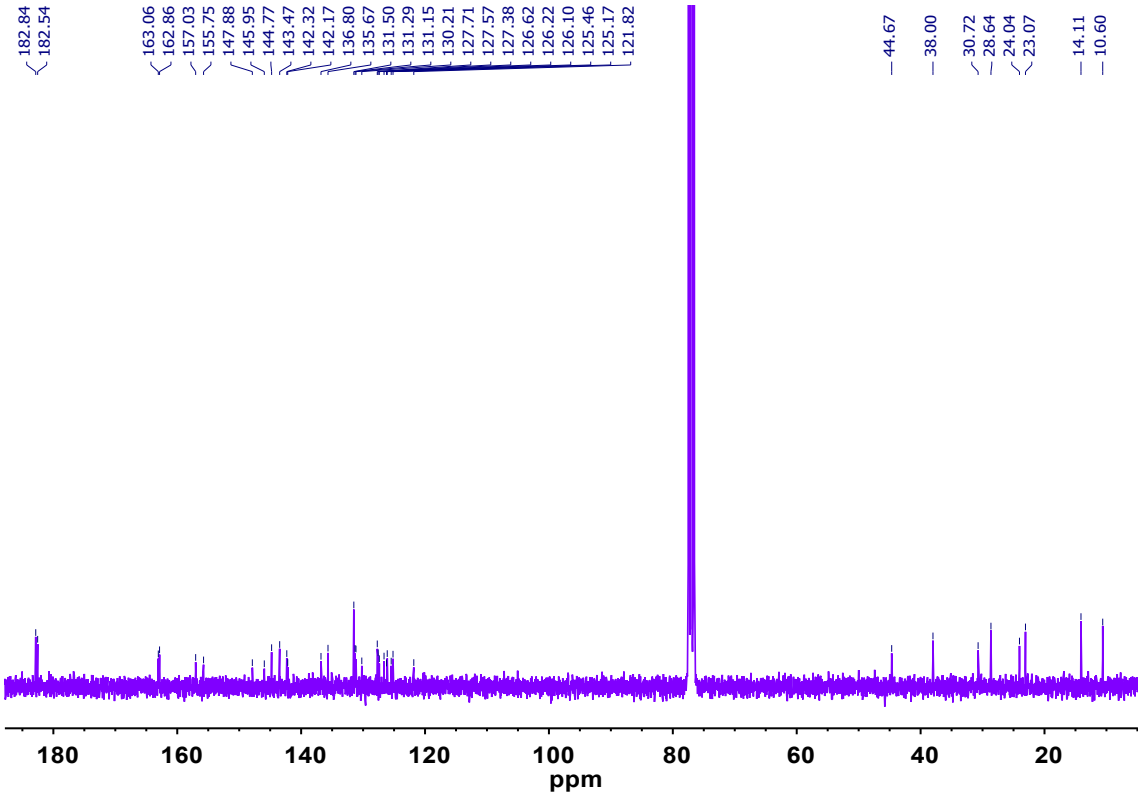

Figure S7. ^{13}C-NMR spectrum of **NDI3T-CHO** in $CDCl_3$.

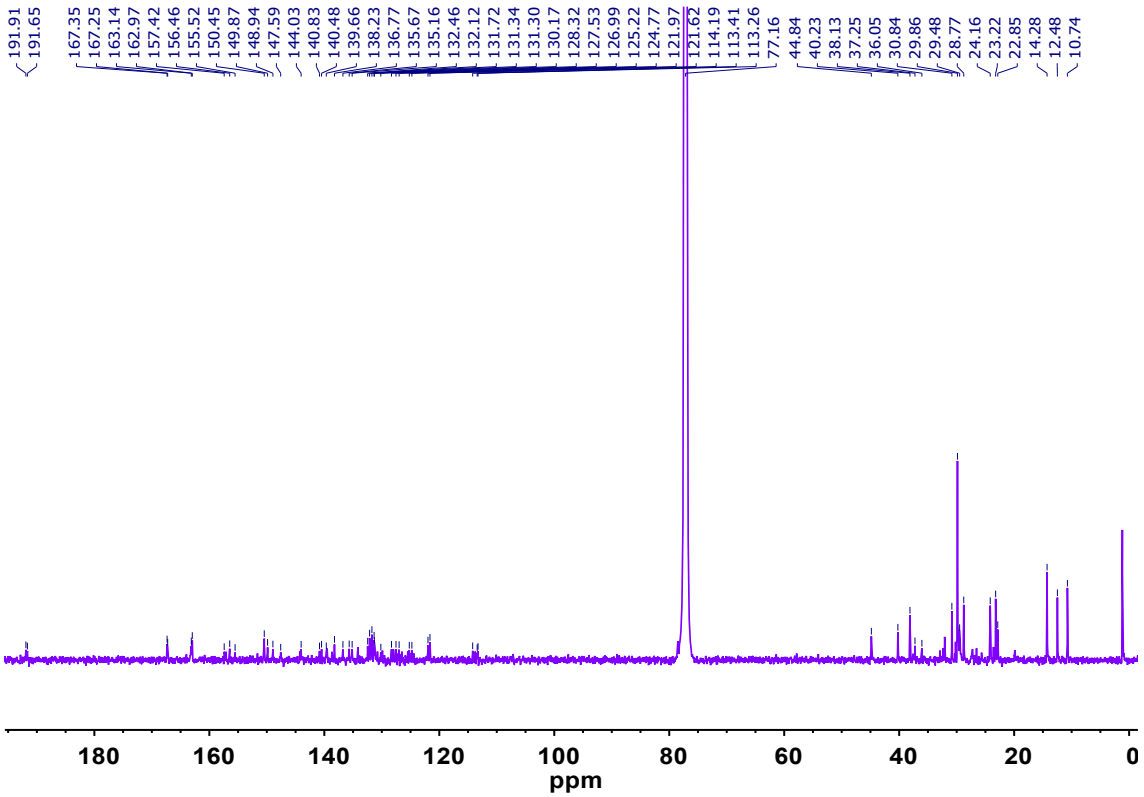

Figure S8. ^{13}C-NMR spectrum of **NDI3T-RD** in $CDCl_3$.

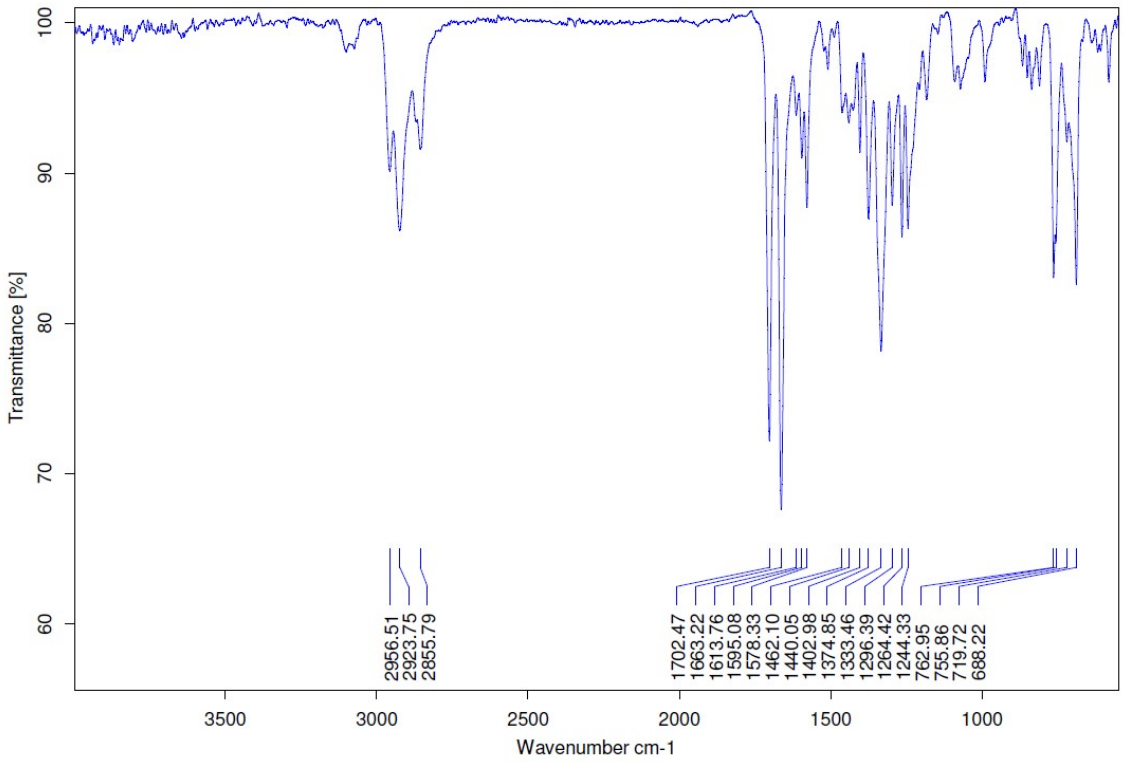

Figure S9. IR spectrum of **NDI3T**.

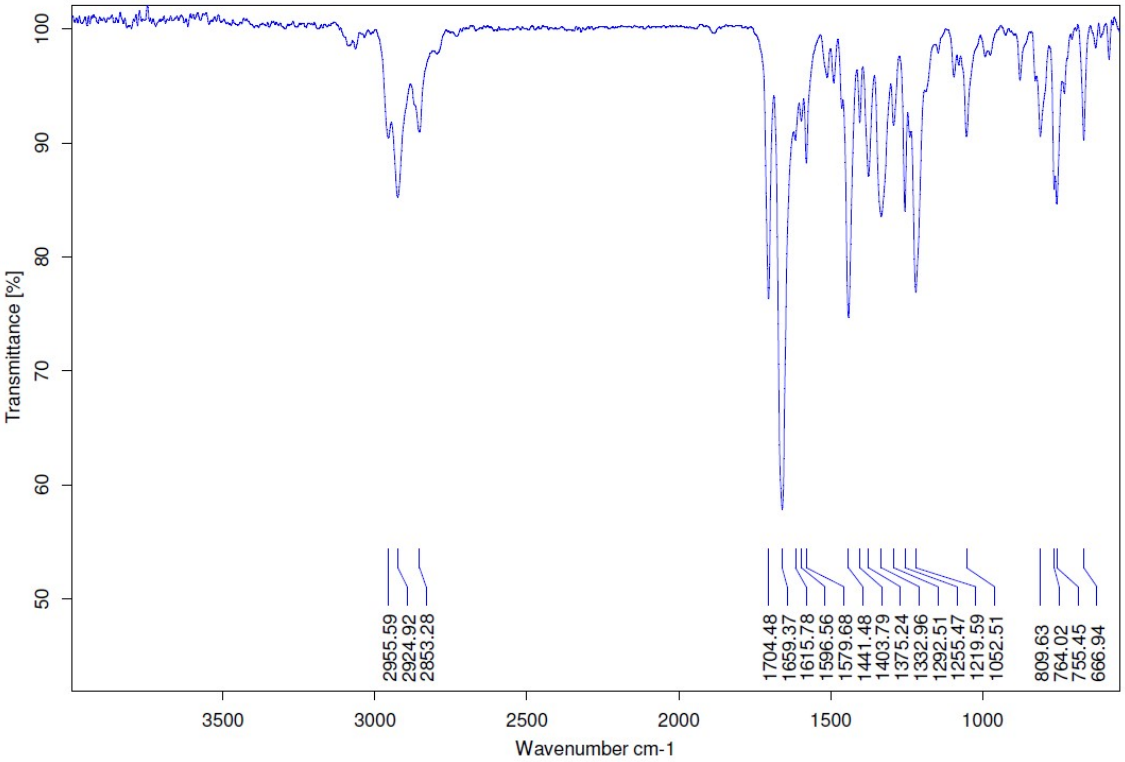

Figure S10. IR spectrum of **NDI3T-CHO**.

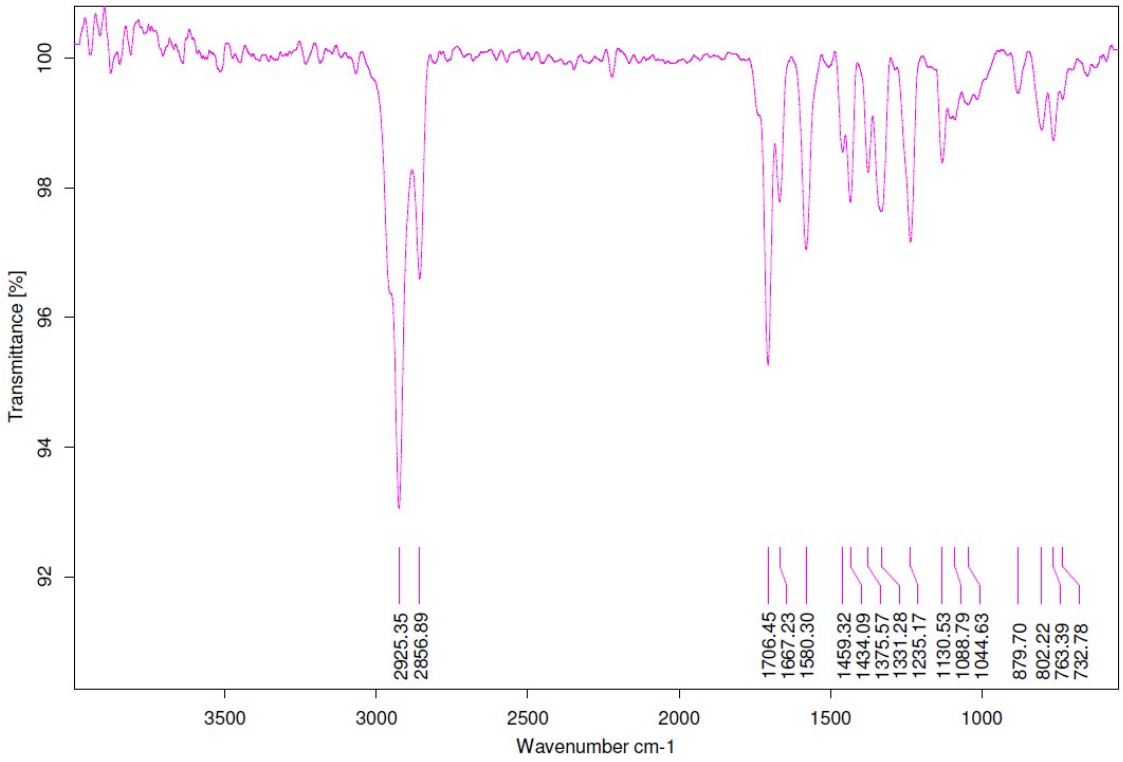

Figure S11. IR spectrum of **NDI3T-RD**.

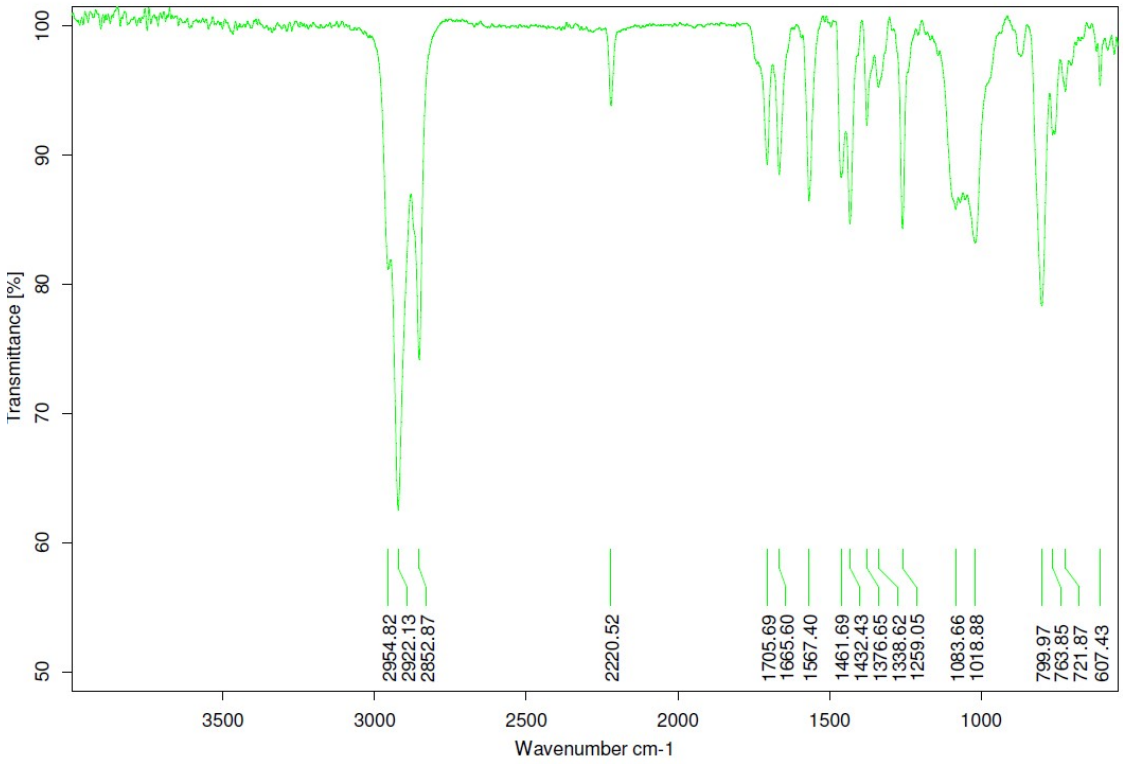

Figure S12. IR spectrum of **NDI3T-DCV**.

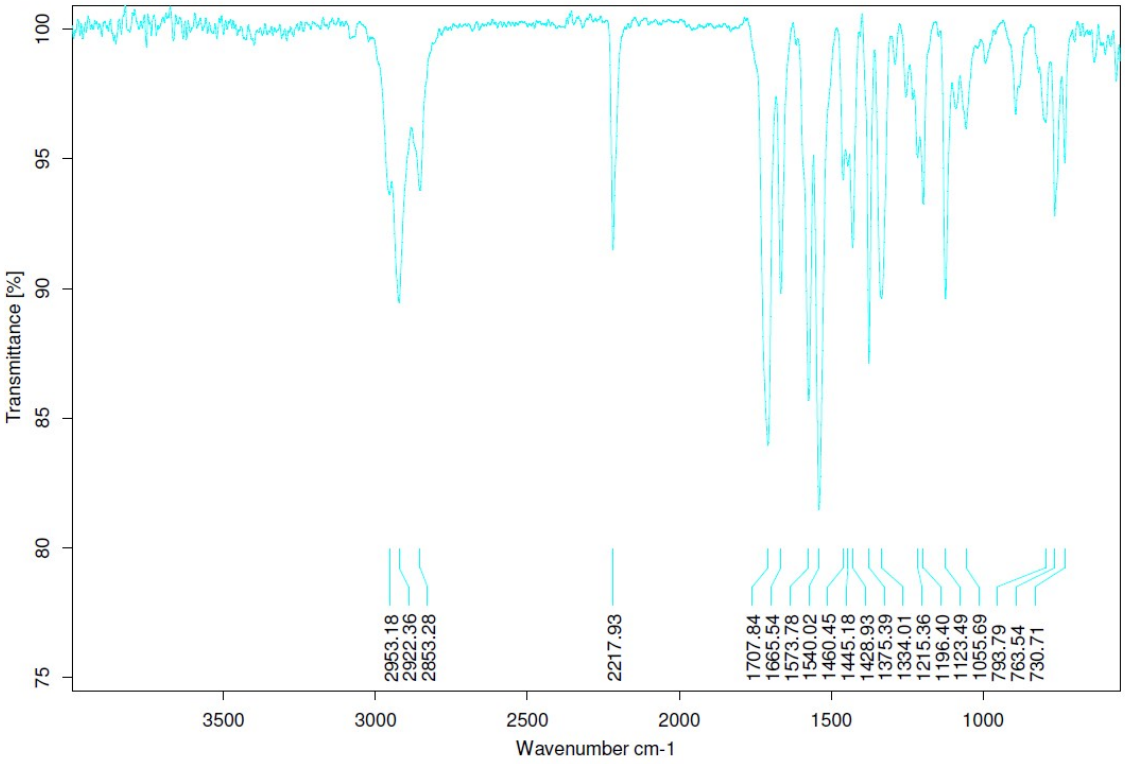

Figure S13. IR spectrum of **NDI3T-RDDCV**.

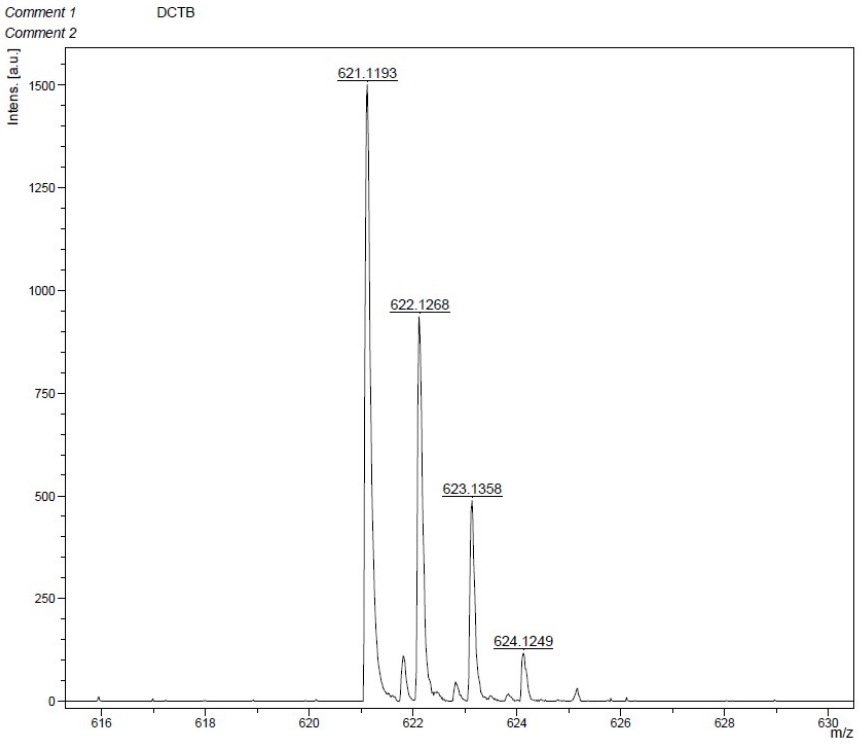

Figure S14. MALDI-HRMS (m/z) spectrum of **NDI3T**.

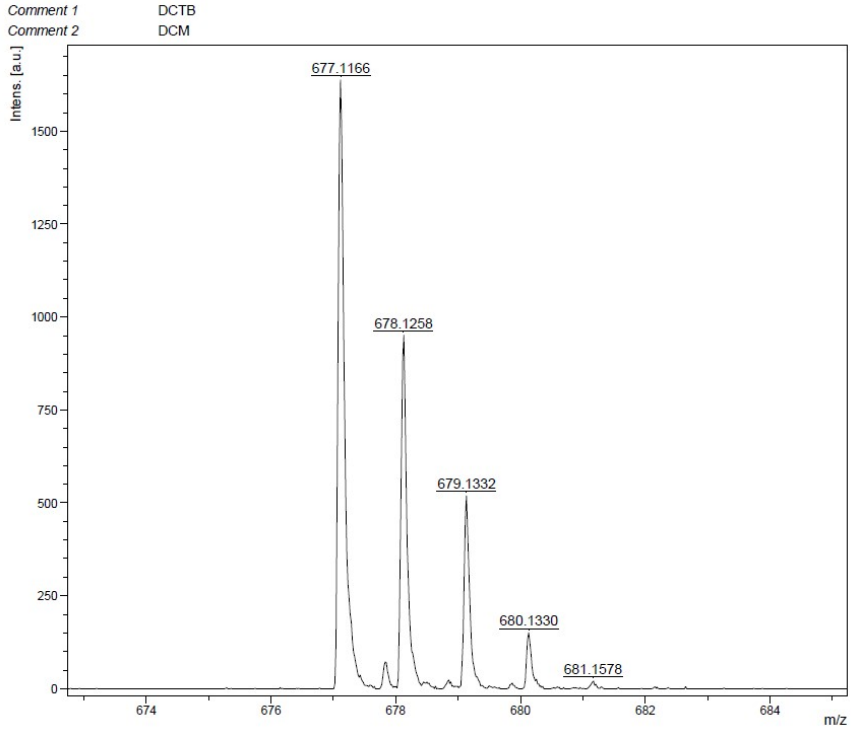

Figure S15. MALDI-HRMS (m/z) spectrum of **NDI3T-CHO**.

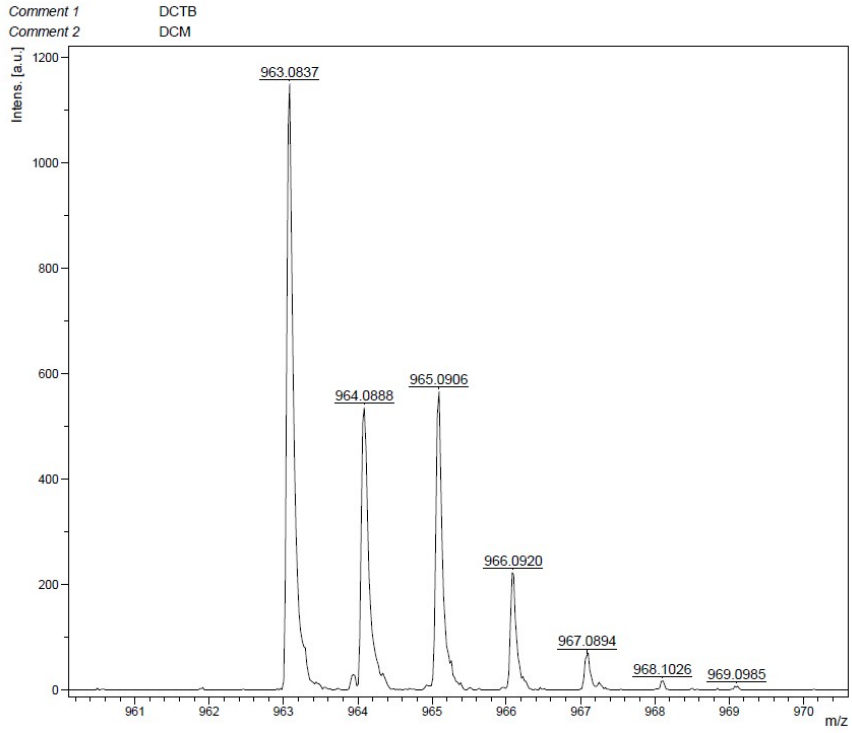

Figure S16. MALDI-HRMS (m/z) spectrum of **NDI3T-RD**.

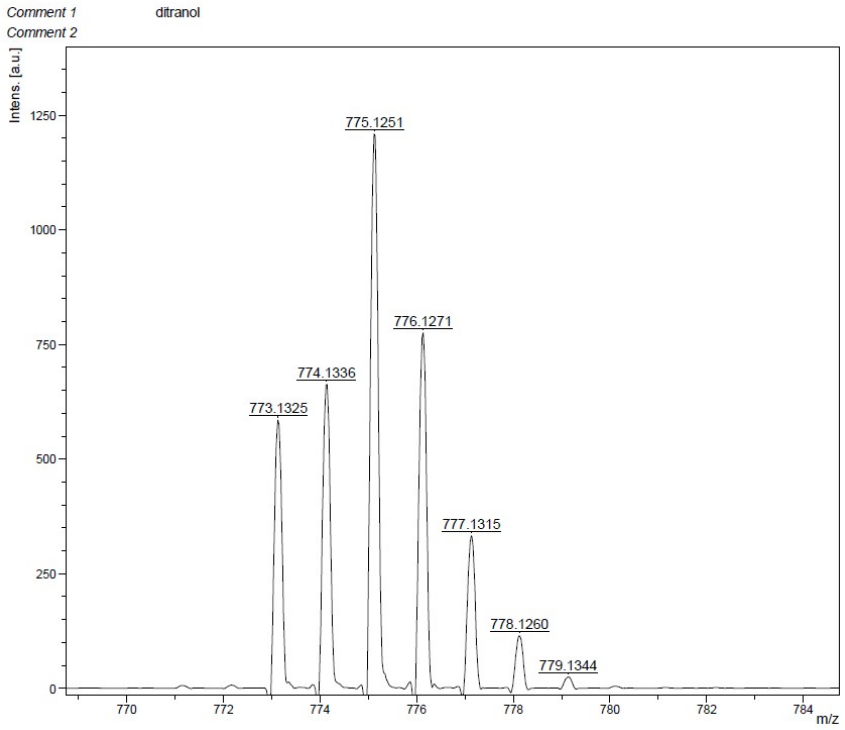

Figure S17. MALDI-HRMS (m/z) spectrum of **NDI3T-DCV**.

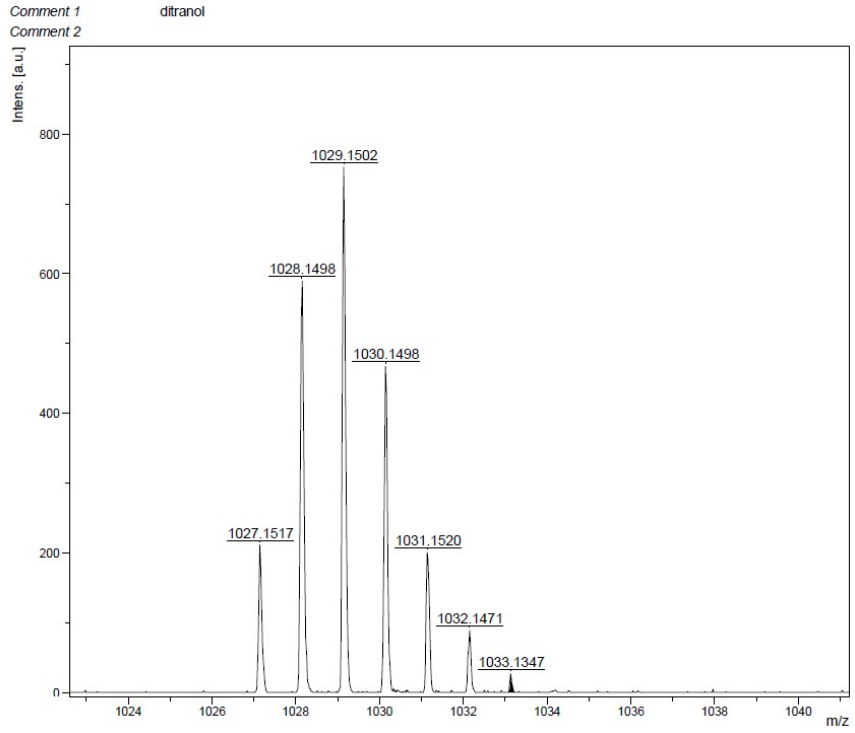

Figure S18. MALDI-HRMS (m/z) spectrum of **NDI3T-RDDCV**.

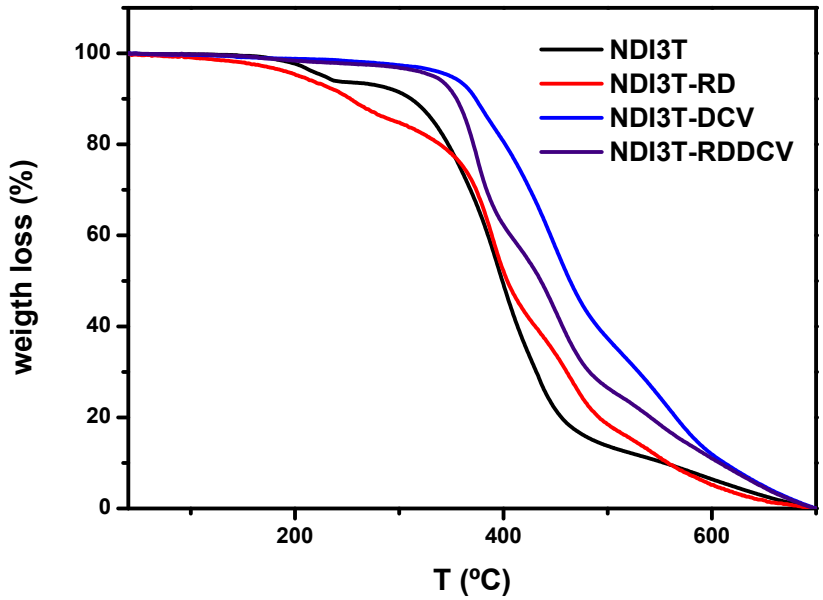

Figure S19. Thermogravimetric analyses of **NDI3T**, **NDI3T-RD, NDI3T-DCV** and **NDI3T-RDDCV** semiconductors**.**

3. DFT and TD-DFT calculations

Theoretical calculations for the NDI monomers were carried out in the frame of density functional theory (DFT), using the B3LYP functional[4-6] and the 6-31G** basis set[7, 8] as implemented in the Gaussian 16 program.[9] 2-decyltetradecyl chains on the N-imide group of NDIs were replaced with isopropyl chains to simplify the calculations, for this reason **NDI3T** acronym is used to simplify the nomenclature. Geometry optimizations were performed without any symmetry constrains. On the basis of the resulting ground-state geometries, harmonic vibrational frequencies were calculated at the same theoretical level. The reorganization energies were calculated directly from the relevant points on the potential energy surfaces by using previously reported standard procedures.

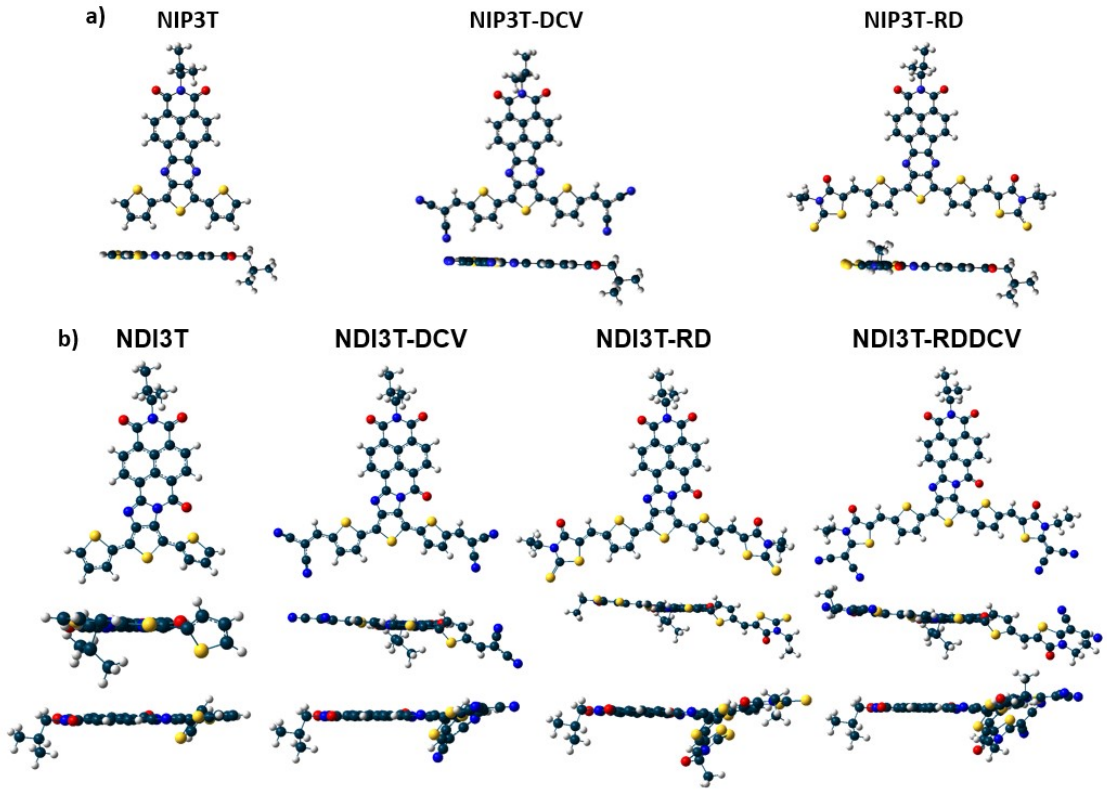

Figure S20. DFT//B3LYP/6-31G** optimized molecular structures of a) NIP and b) NDI systems under study.

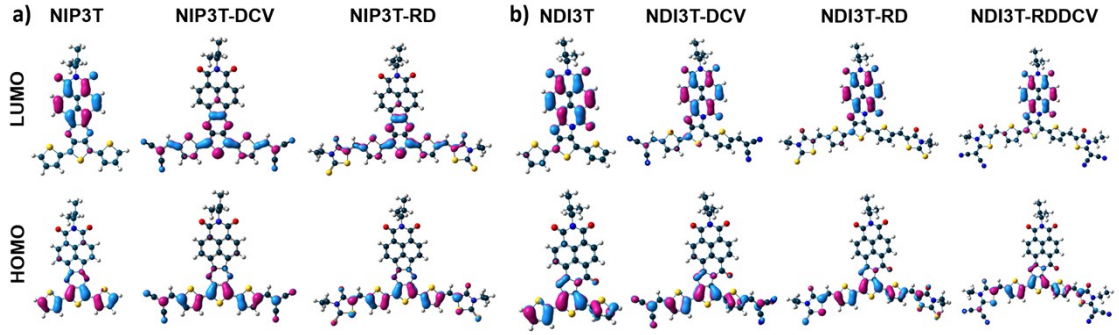

Figure S21 DFT/B3LYP/6-31G** molecular orbital topologies of (a) **NIP3T-X** and (b) **NDI3T-X** systems.

Table S1. HOMO-LUMO gap energies and TDDFT-calculated vertical transition energies with the corresponding description at B3LYP/6-31G** level of theory. The oscillator strength values are given in brackets.

	E_{H-L} (eV)	λ (f) (nm)	Description
NDI3T	1.96	736 (0.22)	HOMO→LUMO (99%)
		468 (0.18)	H-1→LUMO (96%)
		419 (0.23)	HOMO→L+1 (91%), H-2→LUMO (4%), HOMO→L+2 (3%)
		340 (0.24)	H-5→L+1 (17%), HOMO→L+2 (59%)
NDI3T-DCV	2.07	686 (0.31)	HOMO→LUMO (97%), HOMO→L+1 (3%)
		522 (1.16)	HOMO→L+1 (96%), HOMO→LUMO (3%)
		424 (0.29)	H-2→LUMO (62%), H-1→L+1 (18%), HOMO→L+2 (13%)
NDI3T-RD	1.85	781 (0.31)	HOMO→LUMO (99%)
		551 (1.62)	HOMO→L+1 (95%), H-1→LUMO (3%)
		434 (0.29)	H-5→LUMO (73%), H-1→L+1 (13%), H-7→LUMO (3%), H-4→LUMO (4%)
NDI3T-RDDCV	1.93	746 (0.38)	HOMO→LUMO (99%)
		561 (1.19)	HOMO→L+1 (83%), H-1→LUMO (16%)
		554 (0.56)	H-1→LUMO (82%), HOMO→L+1 (15%)
		438 (0.46)	H-3→LUMO (60%), H-1→L+1 (27%), H-4→LUMO (4%), H-2→LUMO (4%)
NIP3T	2.17	657 (0.23)	HOMO→LUMO (98%)
		632 (0.14)	HOMO→L+1 (98%), HOMO→L+2 (3%)
		376 (0.24)	H-1→L+1 (92%), HOMO→L+4 (3%)
		363 (0.31)	H-2→LUMO (90%), H-3→L+1 (3%)
		357 (0.39)	H-3→LUMO (17%), H-1→L+2 (48%) H-3→LUMO (7%), H-4→L+1 (5%)
		328 (0.64)	H-5→L+1 (53%), H-3→L+1 (36%)
NIP3T-DCV	2.00	665 (0.85)	HOMO→LUMO (98%), HOMO→L+2 (3%)
		610 (0.19)	HOMO→L+1 (98%)
		472 (0.58)	HOMO→L+2 (90%), H-2→LUMO (4%), HOMO→LUMO (4%)
		416 (0.50)	H-1→L+2 (32%), HOMO→L+3 (51%), H-3→LUMO (7%), H-2→L+1 (7%)
		410 (0.21)	H-1→L+1 (89%), H-3→L+1 (5%), HOMO→L+2 (2%)
		364 (0.19)	H-3→LUMO (22%), H-2→L++1 (45%)

NIP3T-RD	1.90	725 (1.04)	HOMO→LUMO (98%), HOMO→L+2 (2%)
		681 (0.24)	HOMO→L+1 (98%)
		508 (0.68)	HOMO→L+2 (89%), H-1→L+1 (6%), HOMO→LUMO (2%)
		479 (0.33)	H-1→L+1 (93%), HOMO→L+2 (6%)
		458 (0.33)	H-1→LUMO (20%), HOMO→L+3 (72%) H-4→L+1 (3%)
		370 (0.28)	H-1→L+3 (59%), HOMO→L+4 (36%)

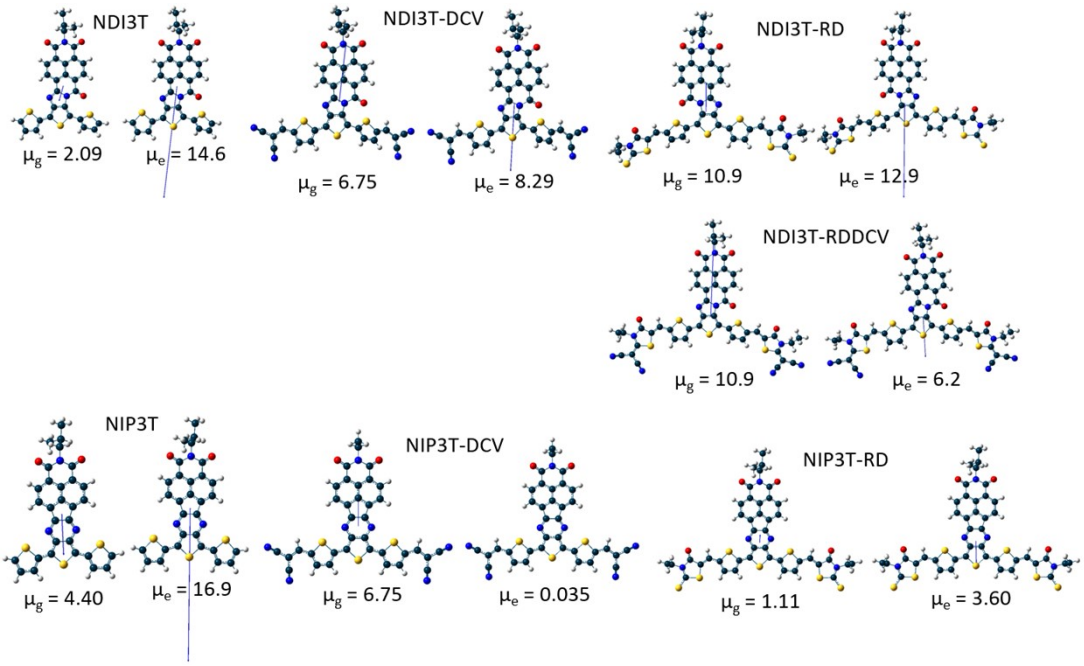

Figure S22. B3LYP/6-31G** calculated dipole moments for **NDI3T-X** and **NIP3T-X** systems of the ground electronic state (μ_g) and the excited state (μ_e).

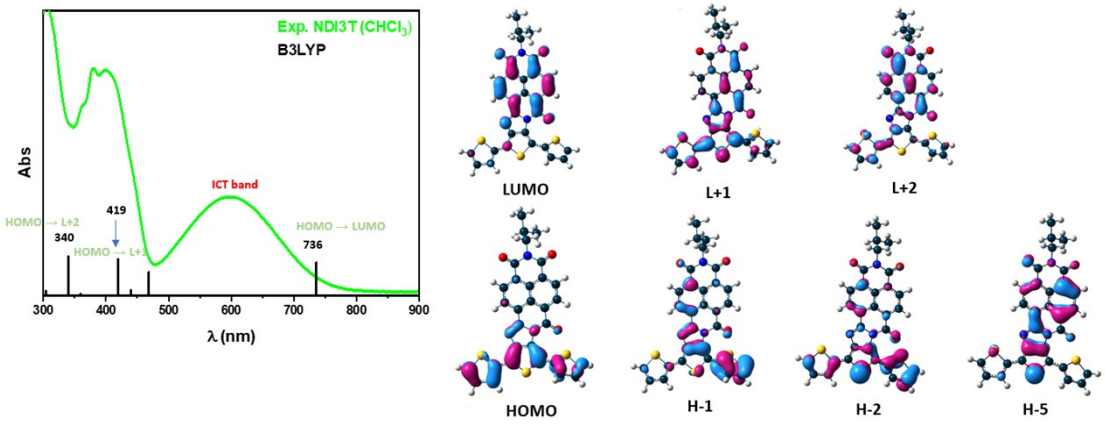

Figure S23. UV-Vis-NIR absorption spectra of **NDI3T** in $CHCl_3$, the TDDFT-B3LYP/6-31G**-calculated vertical transition energies and the molecular orbital topologies.

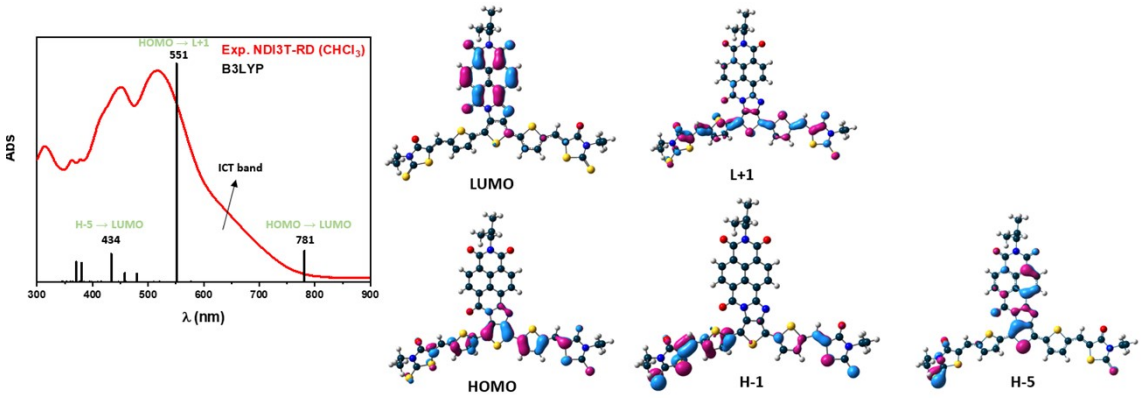

Figure S24. UV-Vis-NIR absorption spectra of **NDI3T-RD** in $CHCl_3$, the TDDFT-B3LYP/6-31G**-calculated vertical transition energies and the molecular orbital topologies.

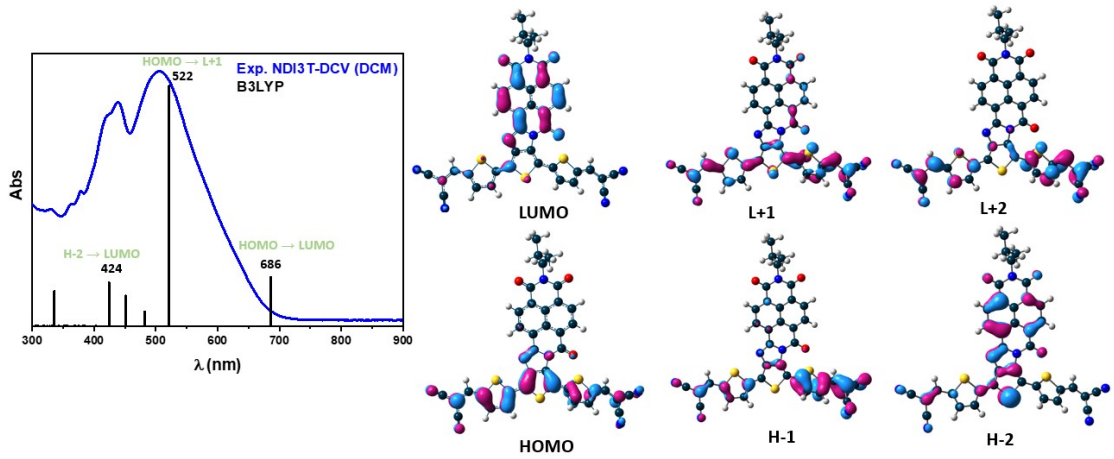

Figure S25. UV-Vis-NIR absorption spectra of **NDI3T-DCV** in $CHCl_3$, the TDDFT-B3LYP/6-31G**-calculated vertical transition energies and the molecular orbital topologies.

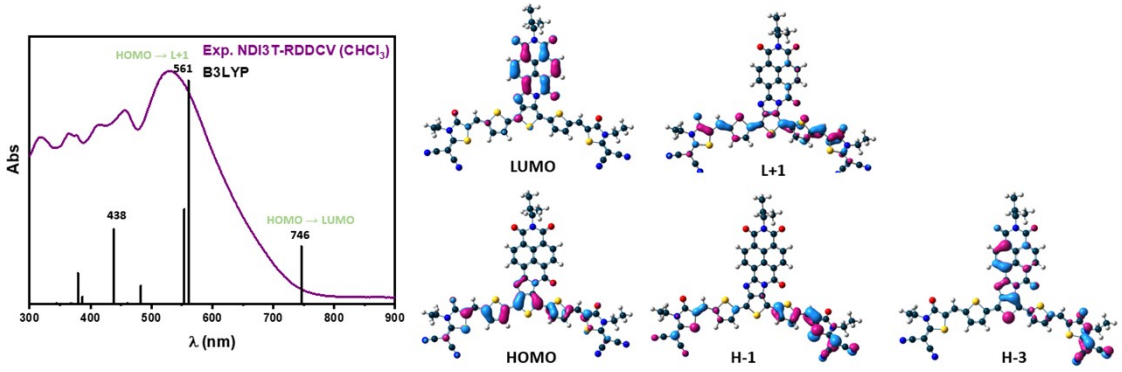

Figure S26. UV-Vis-NIR absorption spectra of **NDI3T-RDDCV** in $CHCl_3$, the TDDFT-B3LYP/6-31G**- calculated vertical transition energies and the molecular orbital topologies.

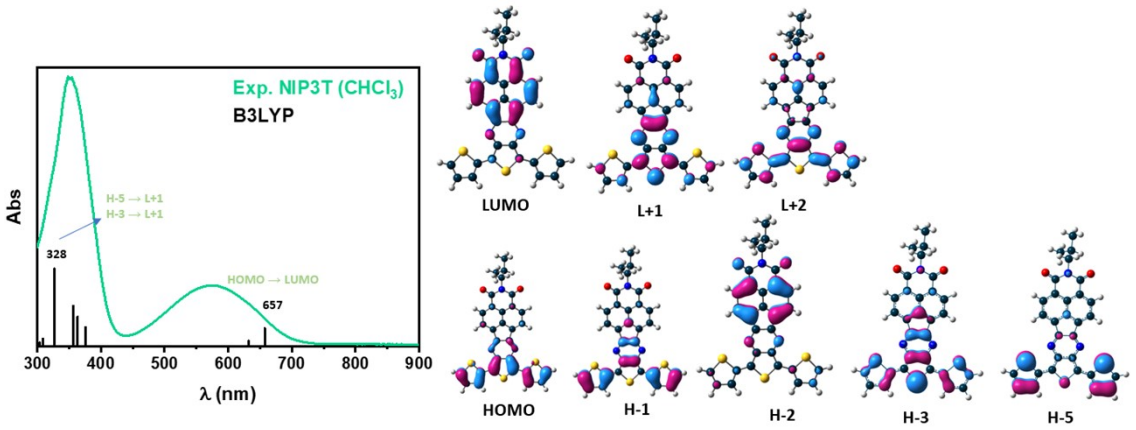

Figure S27. UV-Vis-NIR absorption spectra of **NIP3T** in $CHCl_3$, the TDDFT-B3LYP/6-31G**-calculated vertical transition energies and the molecular orbital topologies.

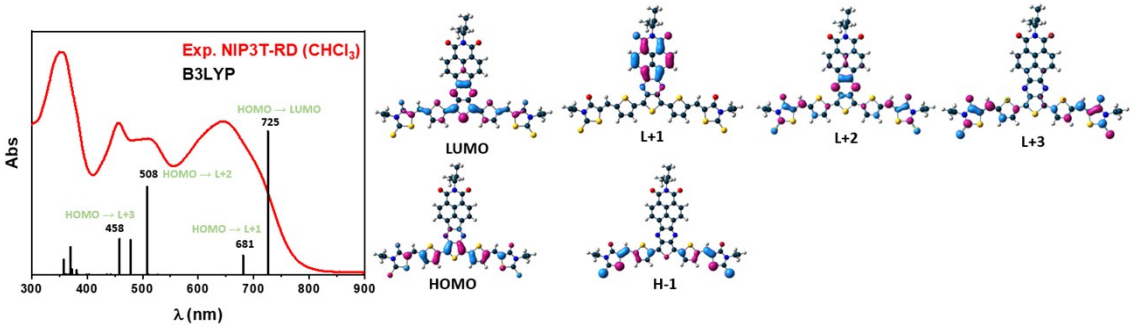

Figure S28. UV-Vis-NIR absorption spectra of **NIP3T-RD** in $CHCl_3$, the TDDFT-B3LYP/6-31G**-calculated vertical transition energies and the molecular orbital topologies.

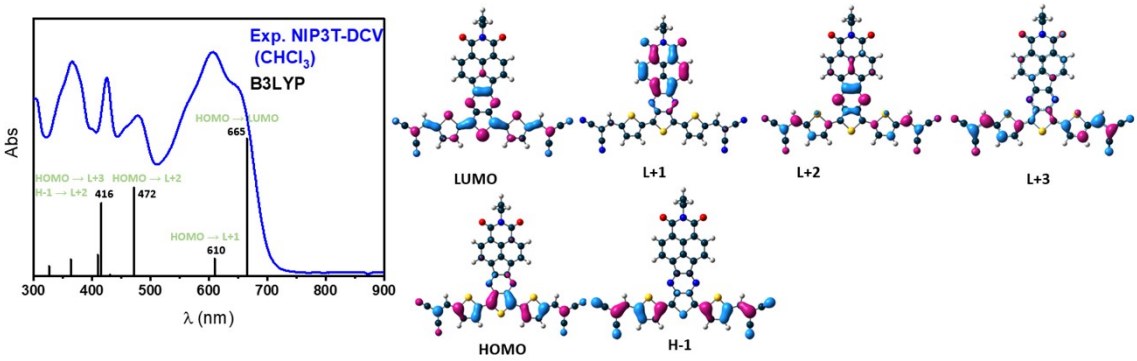

Figure S29. UV-Vis-NIR absorption spectra of **NIP3T-DCV** in $CHCl_3$, the TDDFT-B3LYP/6-31G**-calculated vertical transition energies and the molecular orbital topologies.

4. FT-Raman

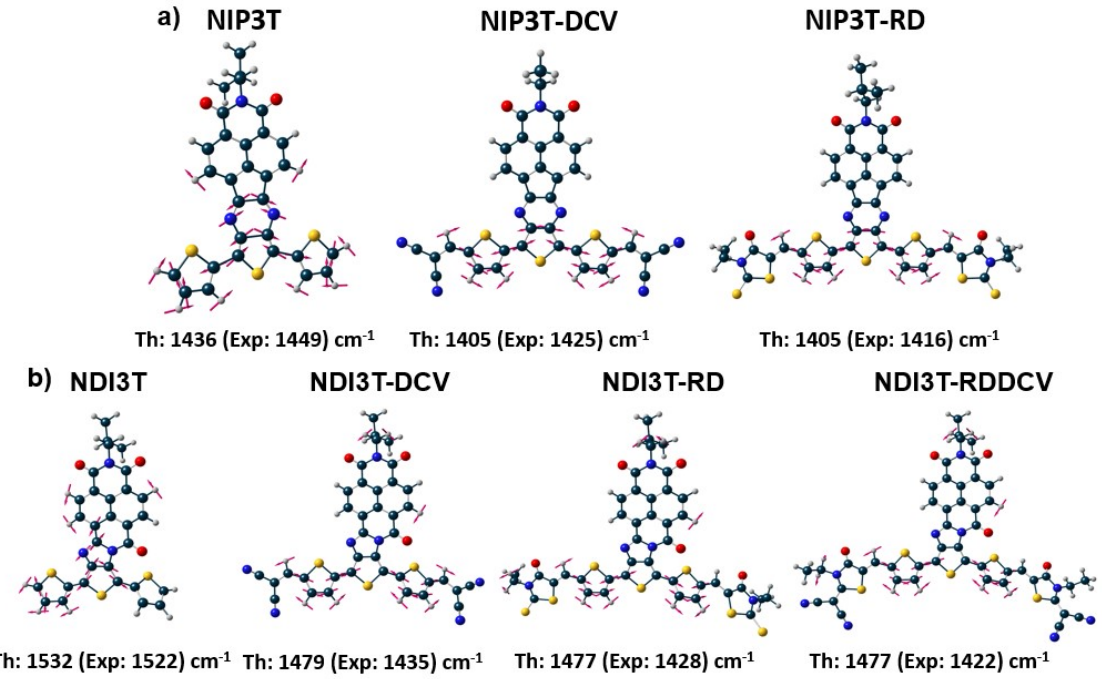

Figure S30. B3LYP/6-31G** predicted eigenvectors for the a) **NIP3T-X** and b) **NDI3T-X** systems.

5. UV-Vis and electrochemical data

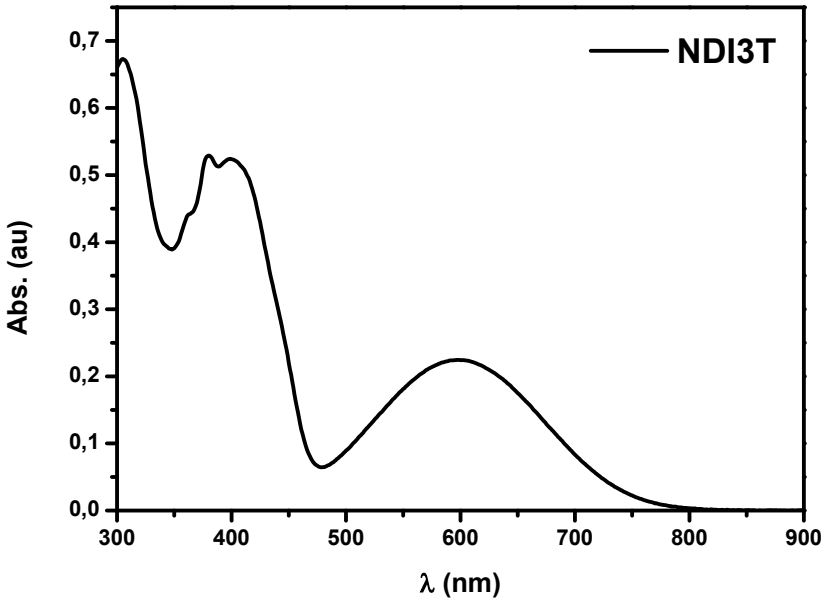

Figure S31. UV-Vis spectra of **NDI3T** 2.75x10^{-5} M in chloroform solution.

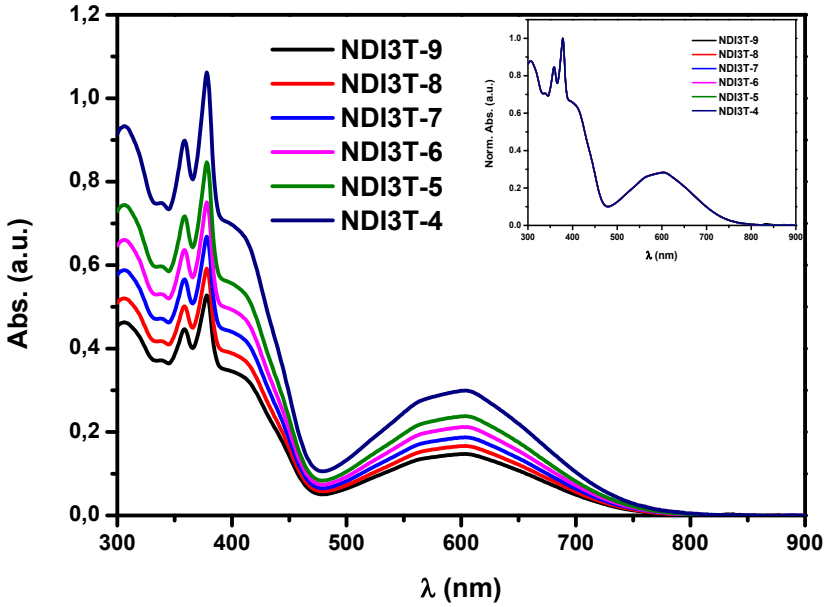

Figure S32. UV-Vis spectra of **NDI3T** dilutions in chloroform solution.

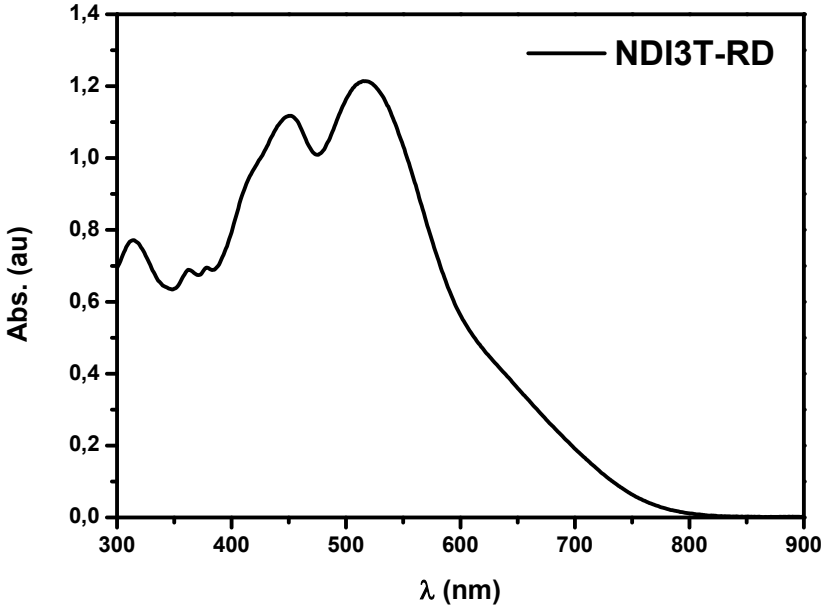

Figure S33. UV-Vis spectra of **NDI3T-RD** 2.75x10^{-5} M in chloroform solution.

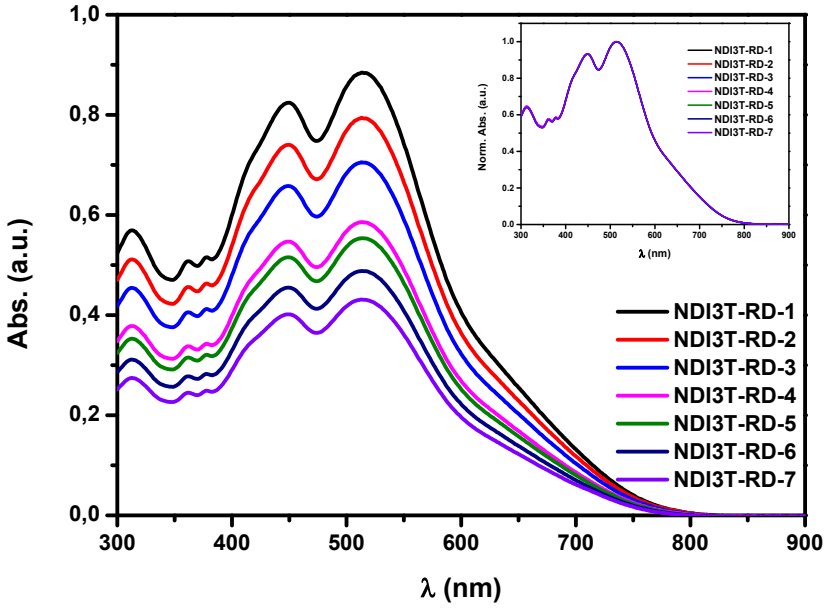

Figure S34. UV-Vis spectra of **NDI3T-RD** dilutions in chloroform solution.

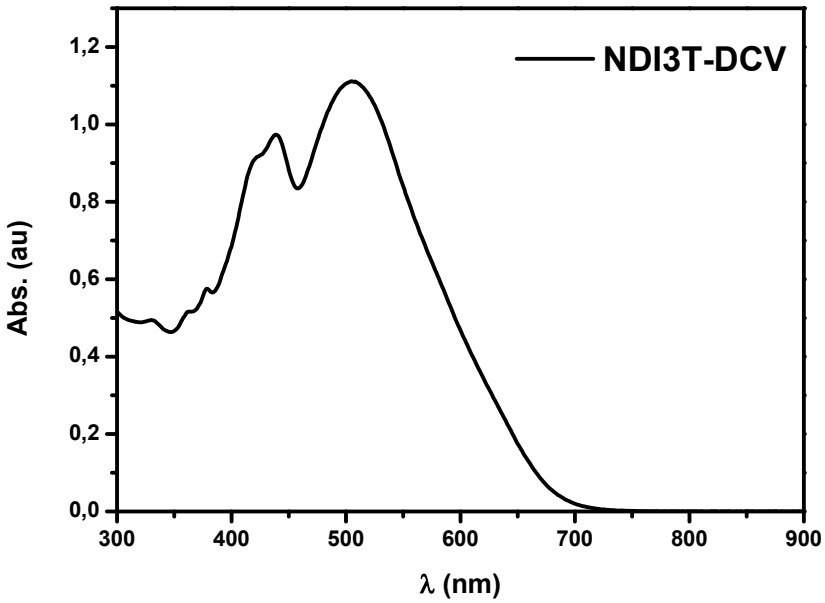

Figure S35. UV-Vis spectra of **NDI3T-DCV** 2.75x10^{-5} M in chloroform solution.

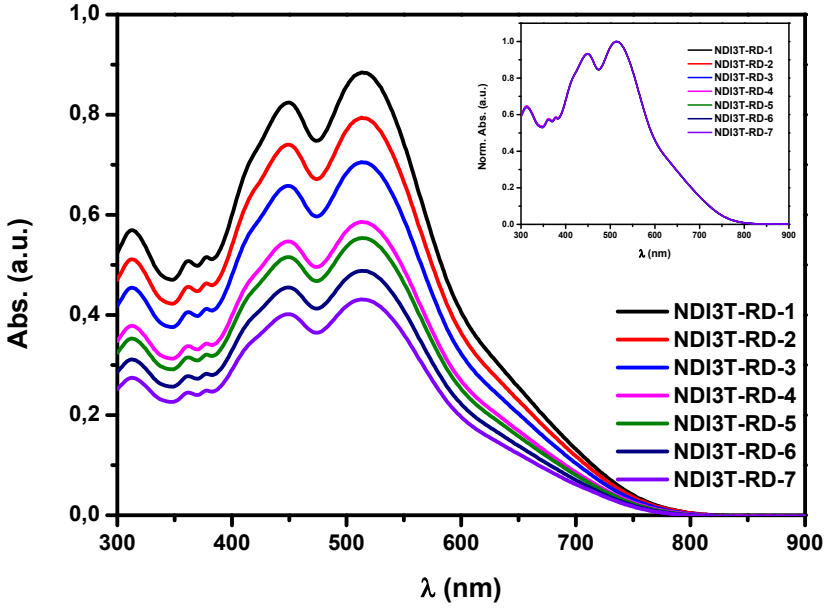

Figure S36. UV-Vis spectra of **NDI3T-DCV** dilutions in chloroform solution.

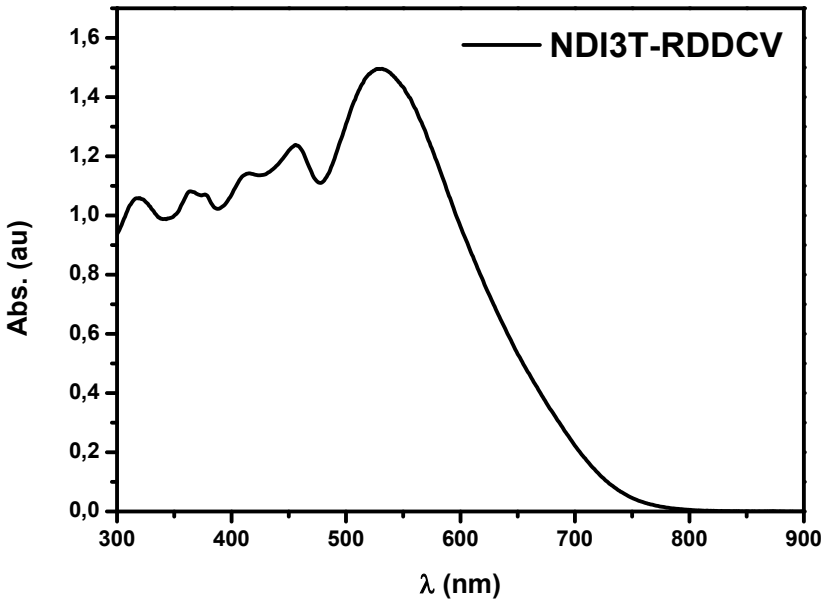

Figure S37. UV-Vis spectra of **NDI3T-RDDCV** 2.75x10^{-5} M in chloroform solution.

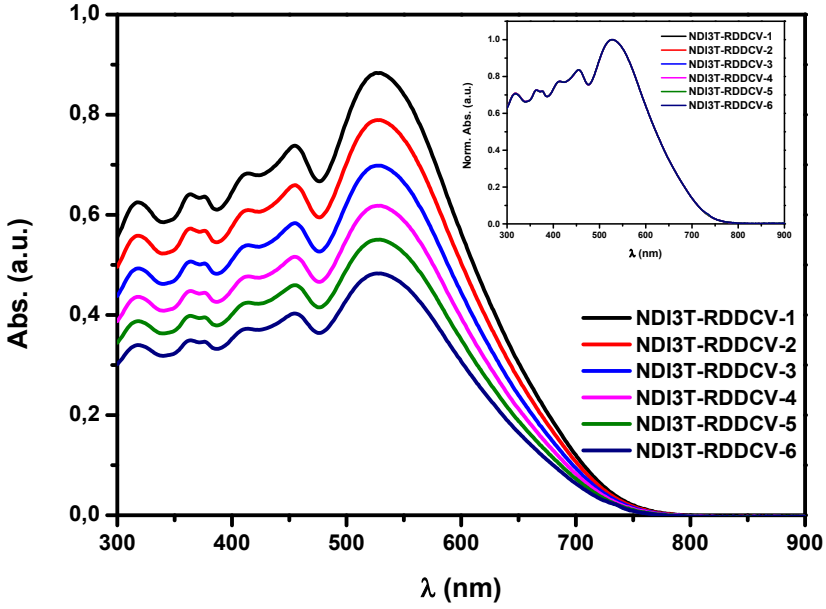

Figure S38. UV-Vis spectra of **NDI3T-RDDCV** dilutions in chloroform solution.

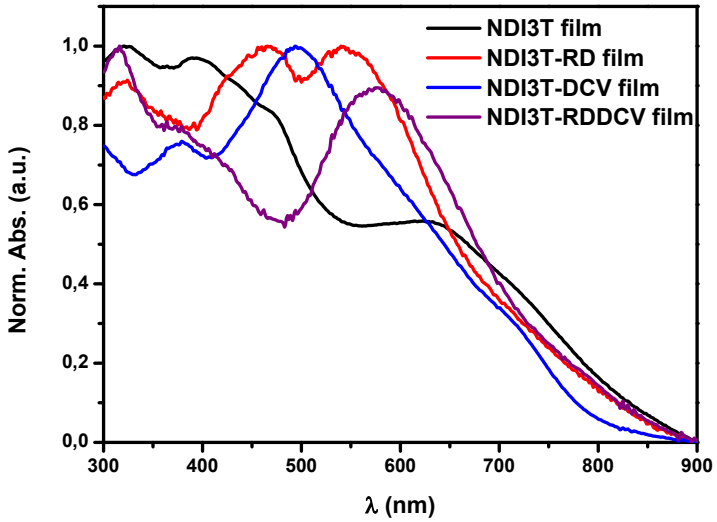

Figure S39. UV-Vis spectra of **NDI3T-X** semiconductors in thin film.

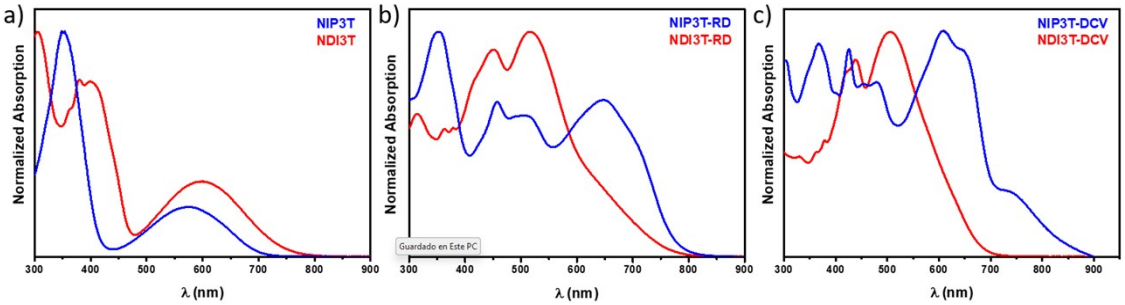

Figure S40X. UV-Vis spectra of **NIP3T-X** semiconductors compared with the NDI3T-X semiconductors.

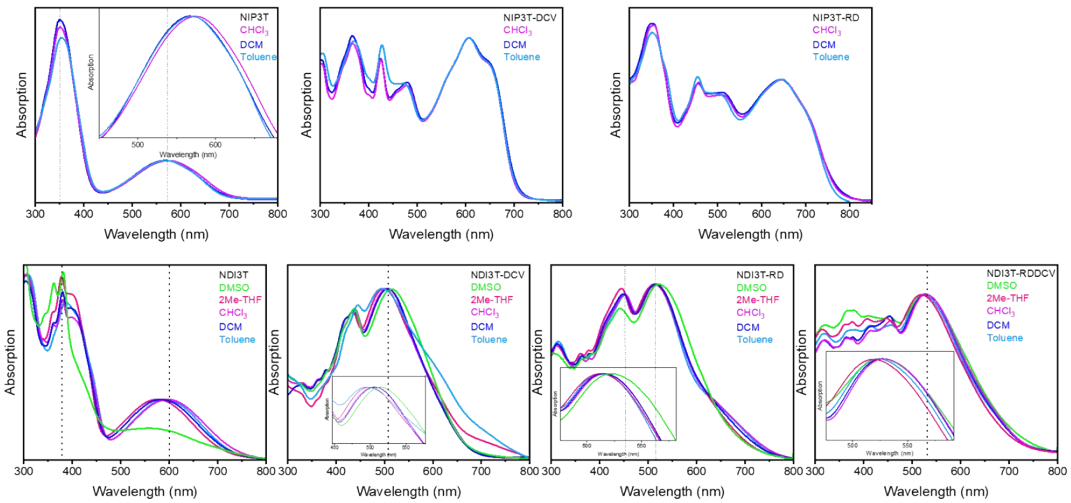

Figure S41. Normalized VV-Vis spectra of **NIP3T-X** and **NDI3T-X** systems in various solvents.

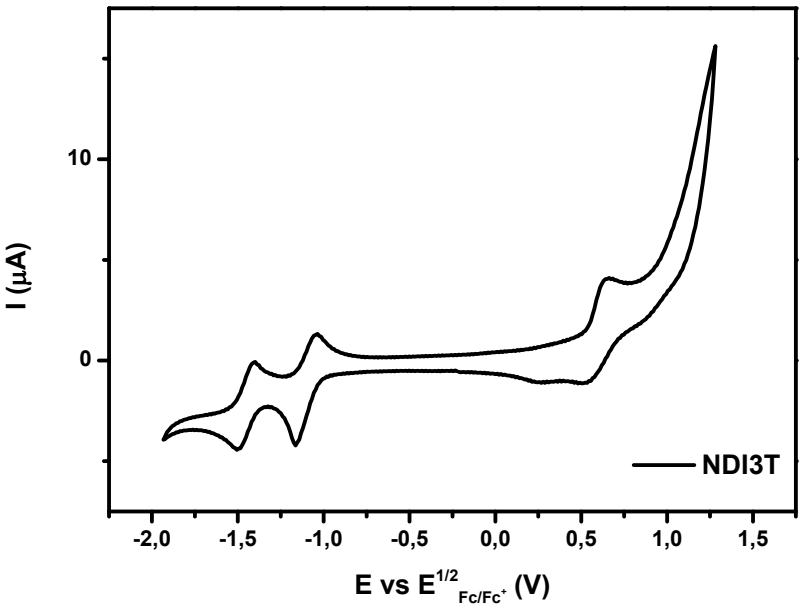

Figure S42. Cyclic voltammetry of **NDI3T** and TBAPF6 0.1M in dichloromethane solution.

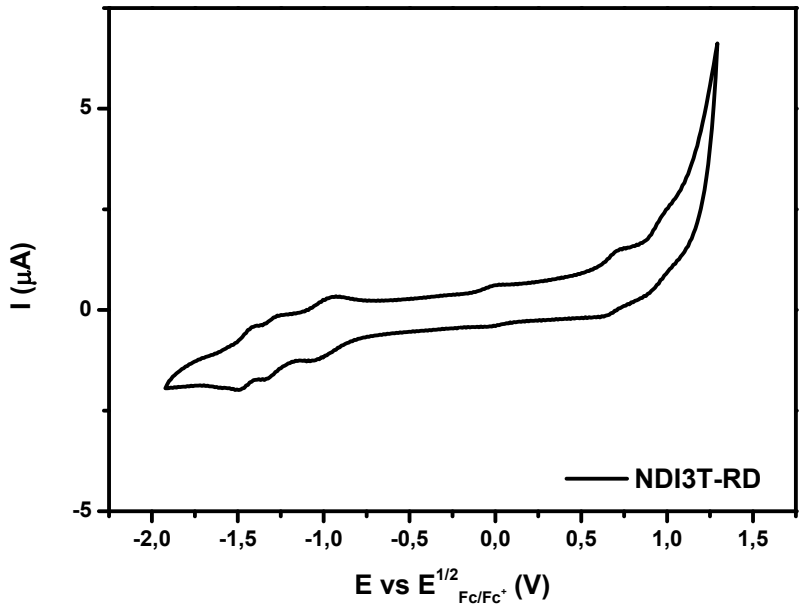

Figure S43. Cyclic voltammetry of **NDI3T-RD** and TBAPF6 0.1M in dichloromethane solution.

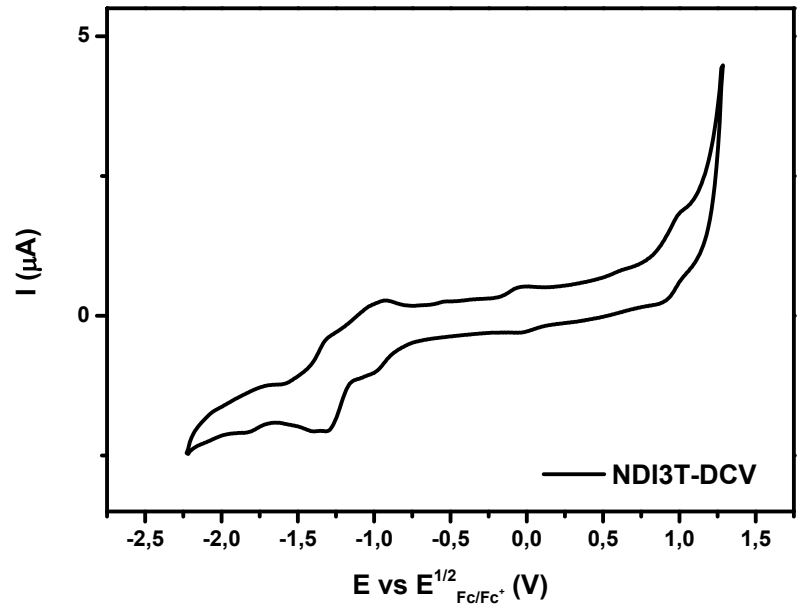

Figure S44. Cyclic voltammetry of **NDI3T-DCV** and TBAPF6 0.1M in dichloromethane solution.

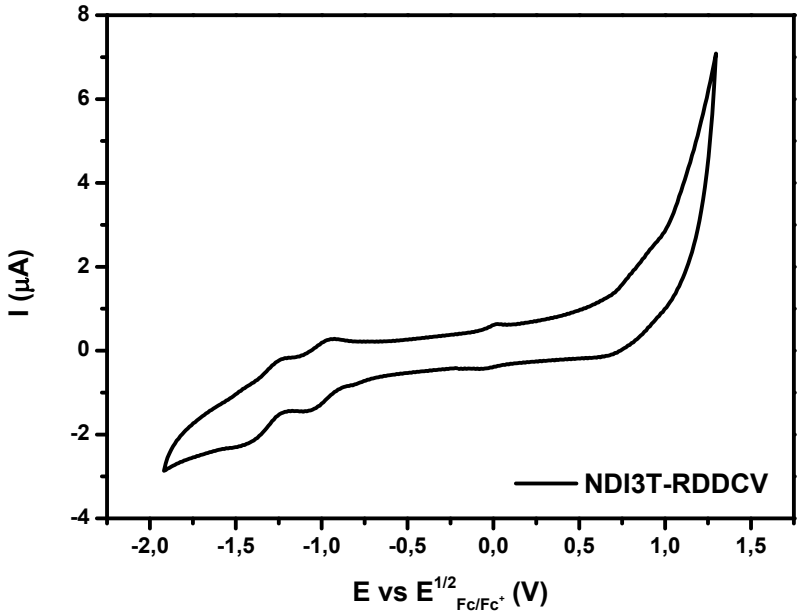

Figure S45. Cyclic voltammetry of **NDI3T-RDDCV** and TBAPF6 0.1M in dichloromethane solution.

6. Spectroelectrochemical measurements

In-situ UV-Vis-NIR spectroelectrochemical studies were conducted in dichloromethane solution (10^{-3}M) at room temperature by using 0.1M NBu_4PF_6 as supporting electrolyte. The diluted solution was introduced in an optically transparent thin-layer electrochemical (OTTLE) cell from Specac, positioned in the sample compartment of a Varian Cary 5000 Spectrophotometer. The OTTLE cell consists of three electrodes: a Pt gauze used as the working electrode (32 wires per cm), a Pt wire used as the counter electrode, and an Ag wire used as the pseudo-reference electrode. This OTTLE is connected to an EC Epsilon potentiostat which controls on the Cary 5000 spectrophotometer. A C3 epsilon potentiostat from BASi which provides the necessary voltage to reduce or oxidized the samples. was used for the oxidation and reduction processes by using an OTTLE cell from Specac. In this cell, the three-electrode system consists of a Pt gauze as working electrode, a Pt wire as the counter electrode and an Ag wire used as the pseudo-reference electrode. The spectra were collected at constant potential electrolysis with an interval of 15 mV. The electrochemical medium used was 0.1 M tetrabutylammonium hexafluorophosphate in dichloromethane at room temperature with sample concentrations of 10^{-3}M.

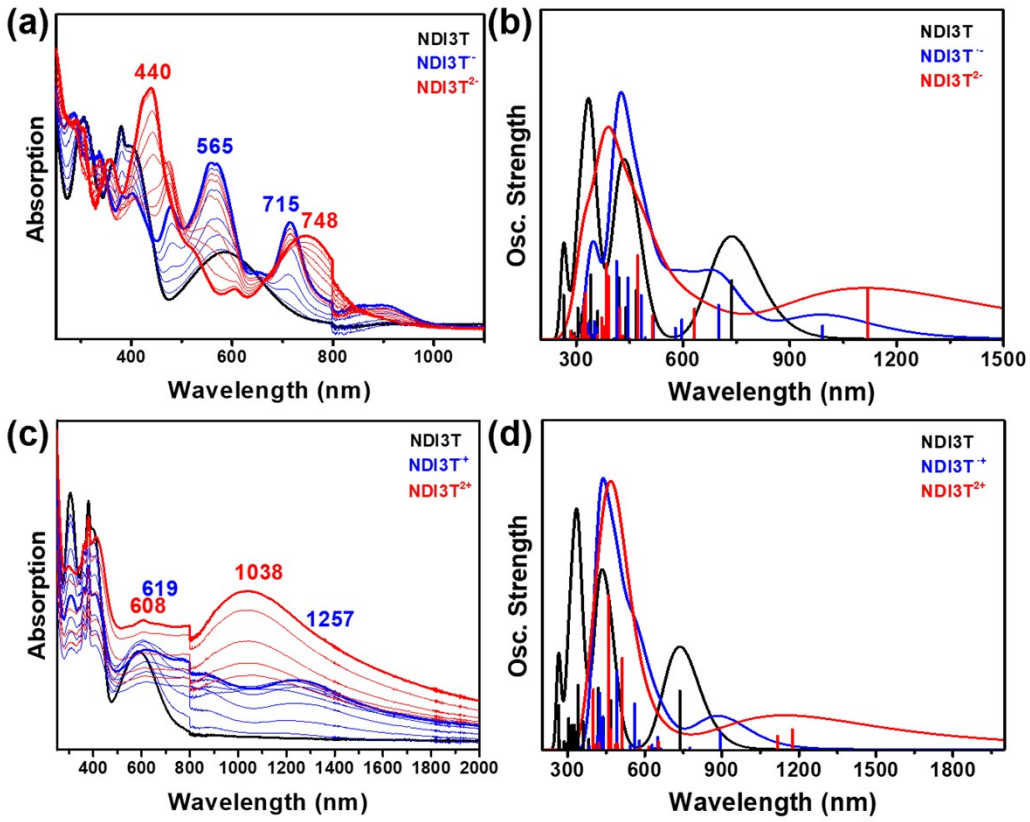

Figure S46. (a),(c) UV-Vis-NIR absorption spectra of **NIP3T** electrochemically reduced and oxidized by progressive increase of the reduction and oxidation potentials, respectively; (b),(d) TDDFT-B3LYP/6-31G**-calculated vertical transition energies.

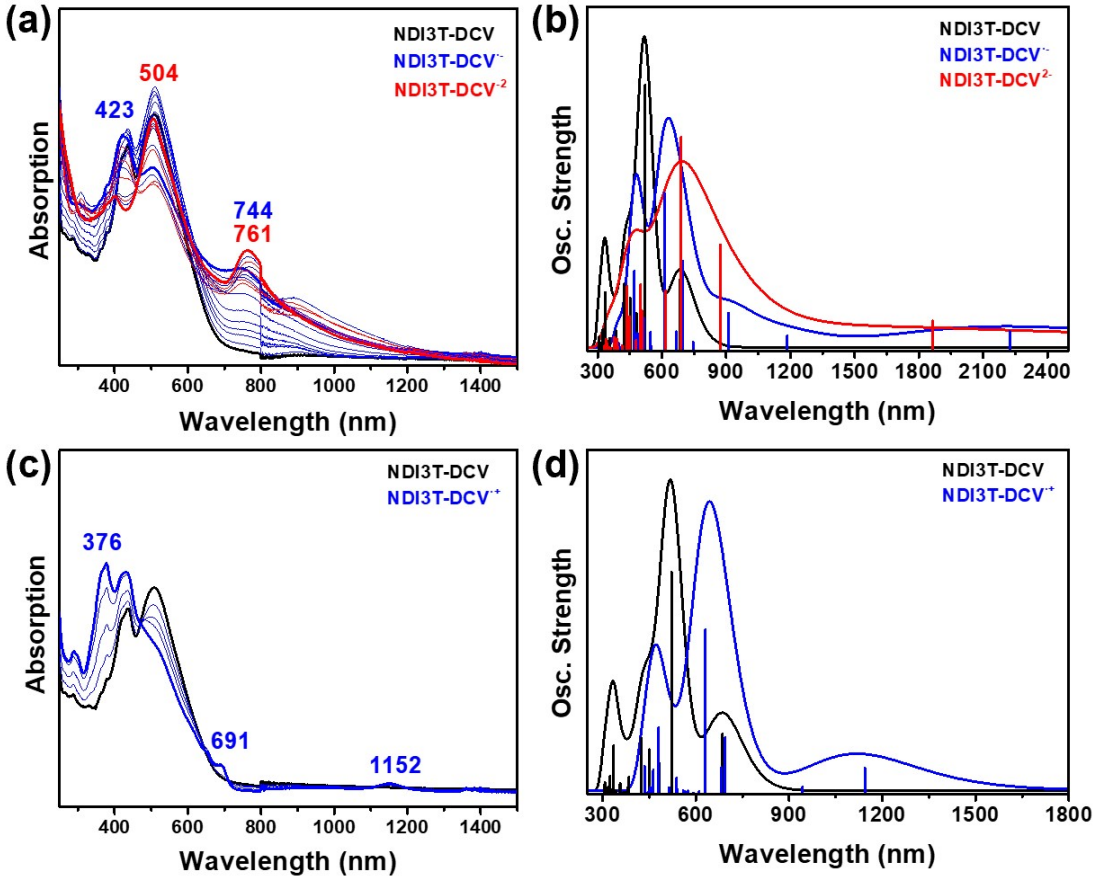

Figure S47. (a),(c) UV-Vis-NIR absorption spectra of **NIP3T-DCV** electrochemically reduced and oxidized by progressive increase of the reduction and oxidation potentials, respectively; (b),(d) TDDFT-B3LYP/6-31G**-calculated vertical transition energies.

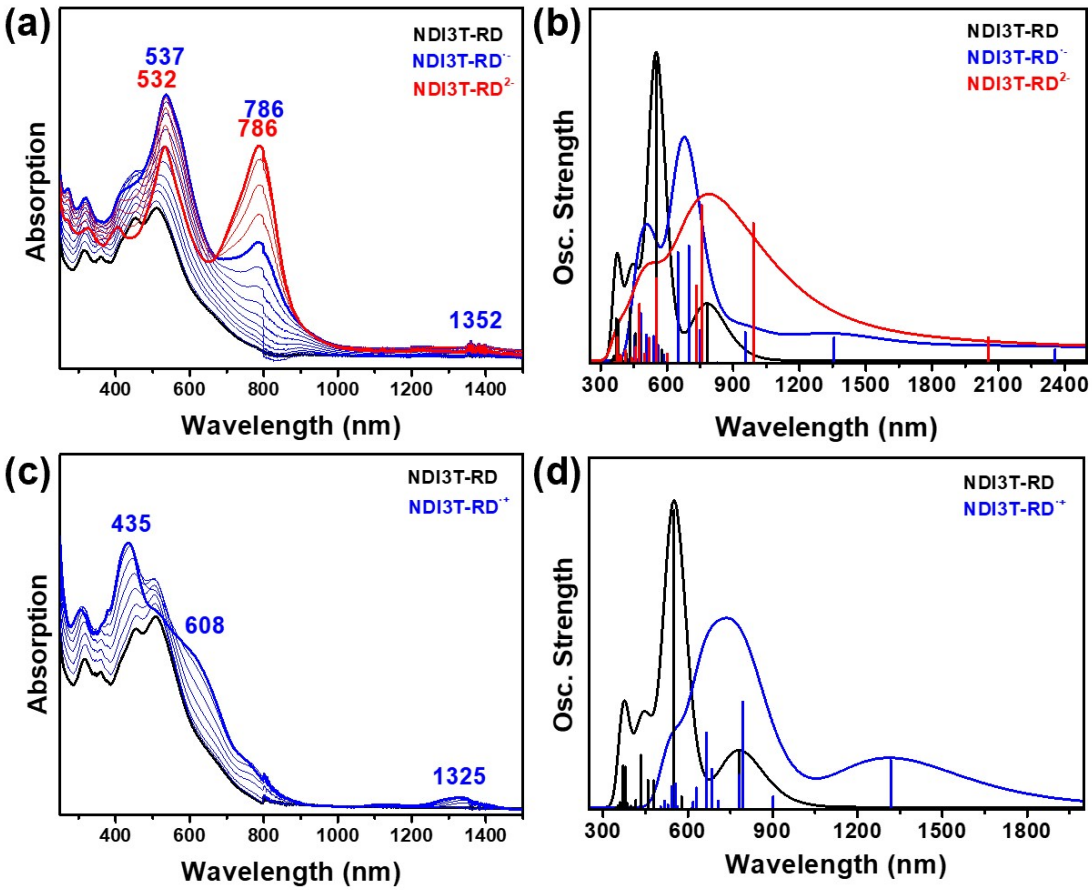

Figure S48. (a),(c) UV-Vis-NIR absorption spectra of **NIP3T-RD** electrochemically reduced and oxidized by progressive increase of the reduction and oxidation potentials, respectively; (b),(d) TDDFT-B3LYP/6-31G**-calculated vertical transition energies.

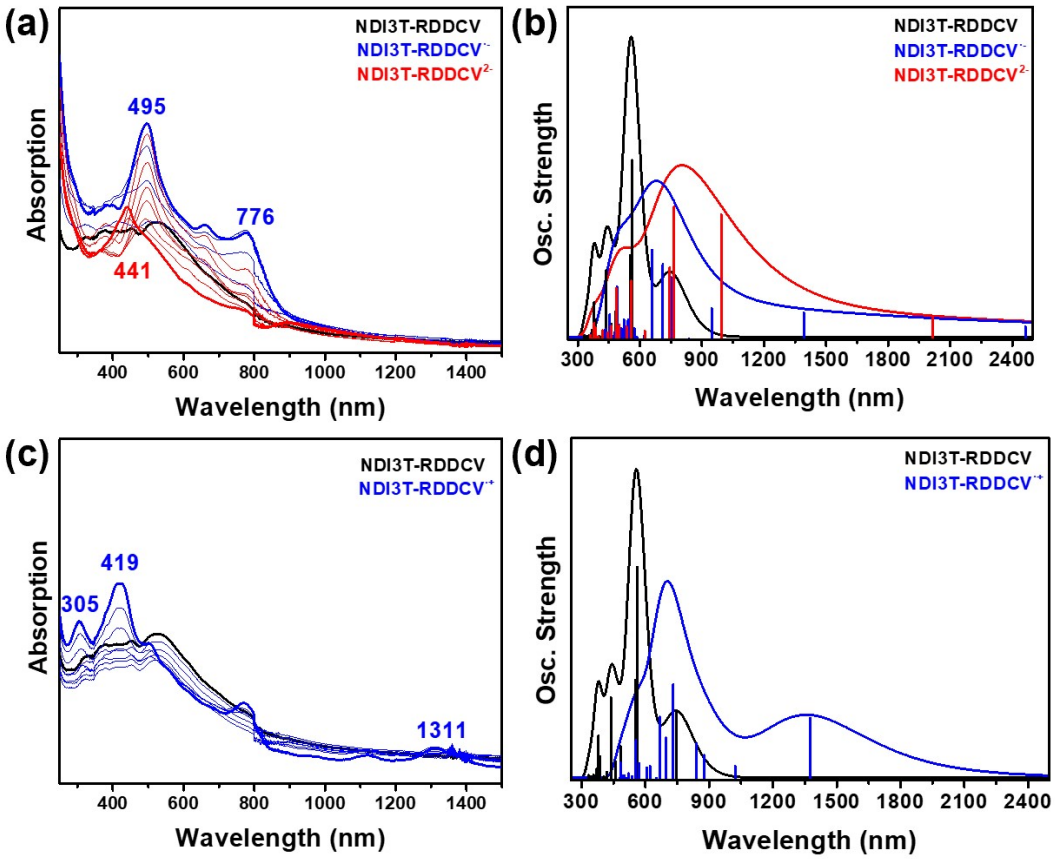

Figure S49. (a),(c) UV-Vis-NIR absorption spectra of **NIP3T-RDDCV** electrochemically reduced and oxidized by progressive increase of the reduction and oxidation potentials, respectively; (b),(d) TDDFT-B3LYP/6-31G**-calculated vertical transition energies.

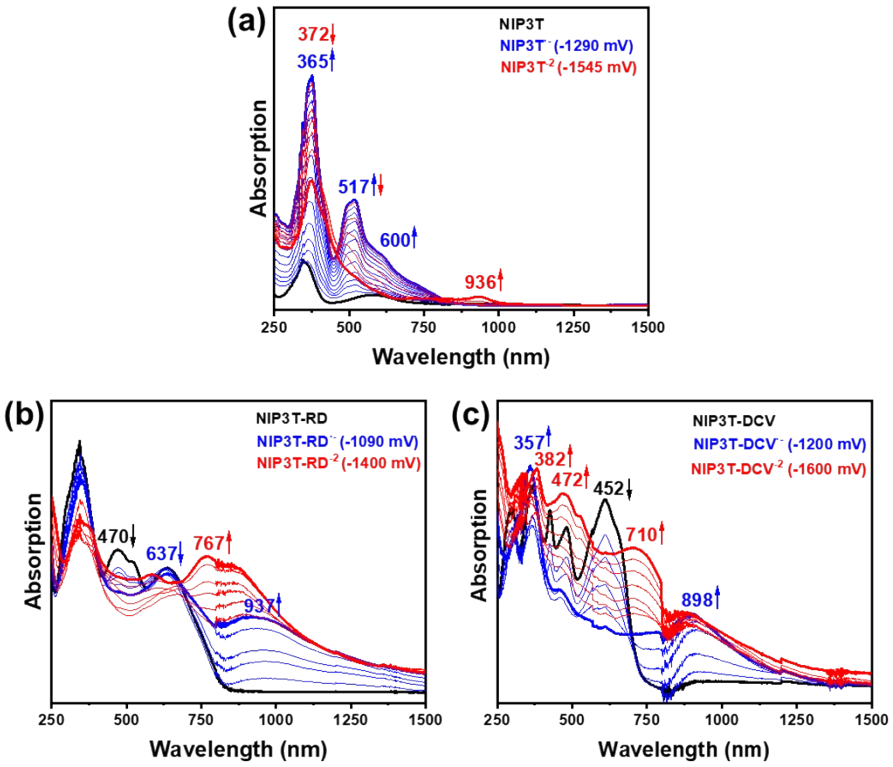

Figure S50. UV-Vis-NIR absorption spectra recorded by electrochemical reduction of (a) **NIP3T**, (b) **NIP3T-RD** and (c) **NIP3T-RDCV** in dichloromethane in presence of Bu_4NBF_4 as supporting electrolyte within an OTTLE cell.

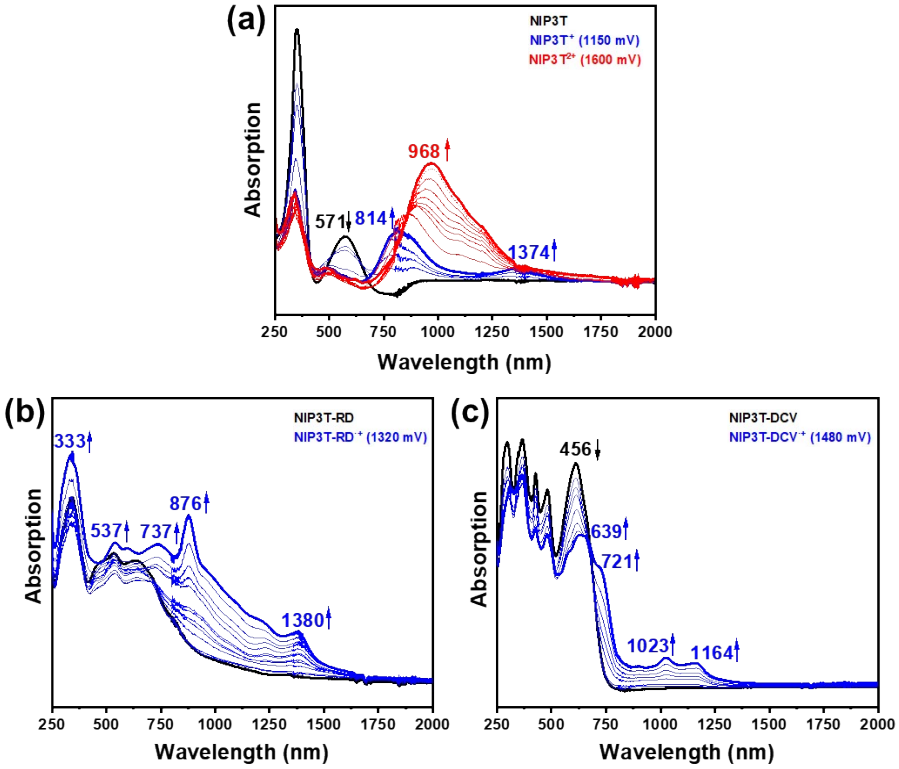

Figure S51. UV-Vis-NIR absorption spectra recorded by electrochemical oxidation of (a) **NIP3T**, (b) **NIP3T-RD** and (c) **NIP3T-DCV** in dichloromethane in presence of Bu_4NBF_4 as supporting electrolyte within an OTTLE cell.

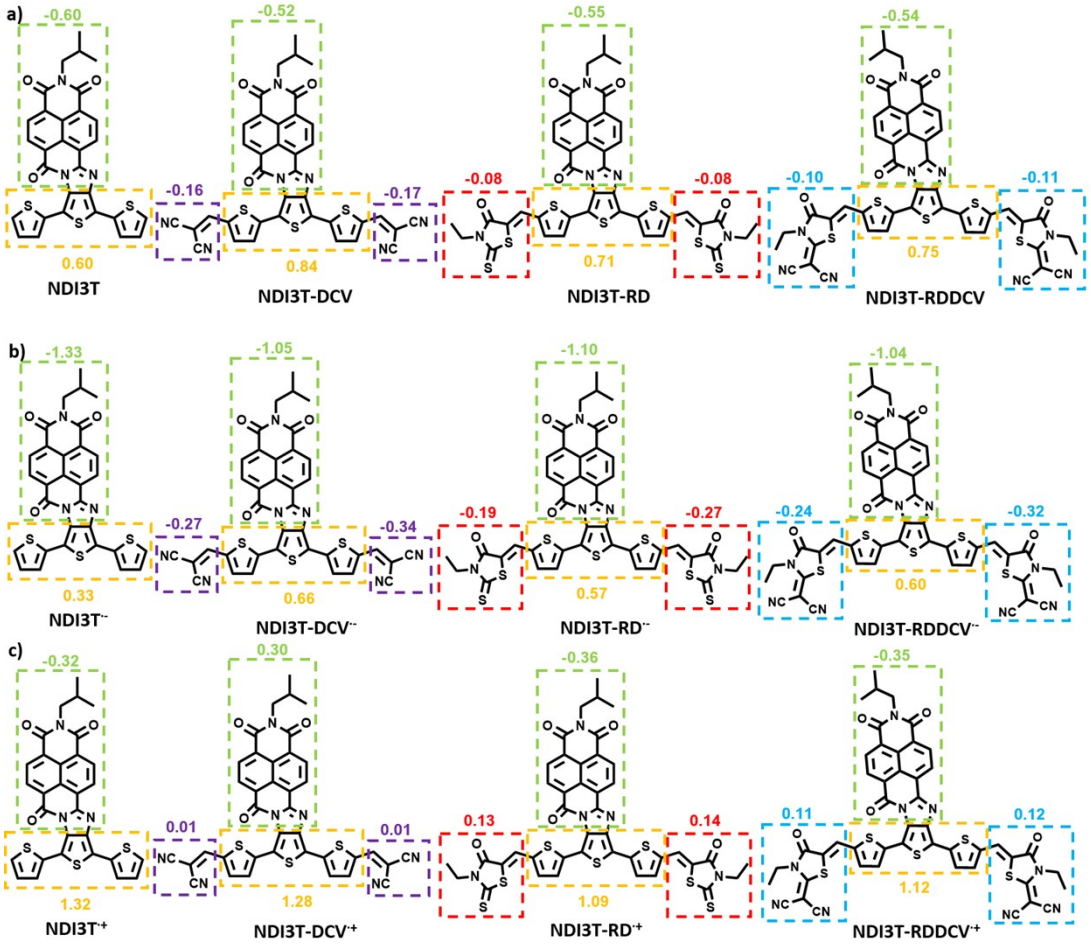

Figure S52. B3LYP/6-31G**-charge distributions for **NDI3T**, **NIP3T-DCV**, **NIP3T-Rd** and **NIP3T-RDDCV** as (a) neutral (b) anion and (c) cation.

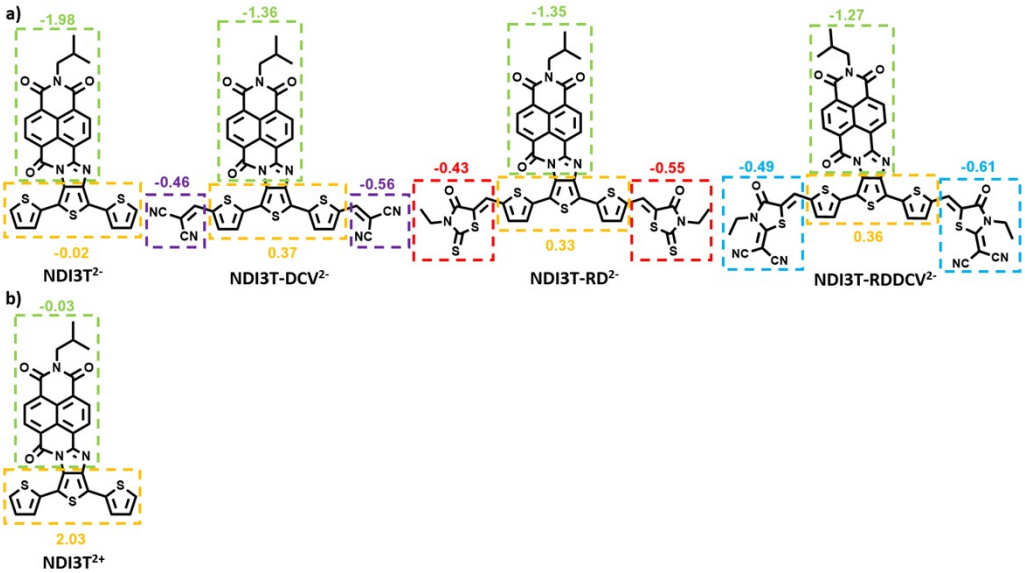

species.

Figure S53. B3LYP/6-31G**-charge distributions for **NDI3T**, **NIP3T-DCV**, **NIP3T-Rd** and d) **NIP3T-RDDCV** as (a) dianion and(b) dication species.

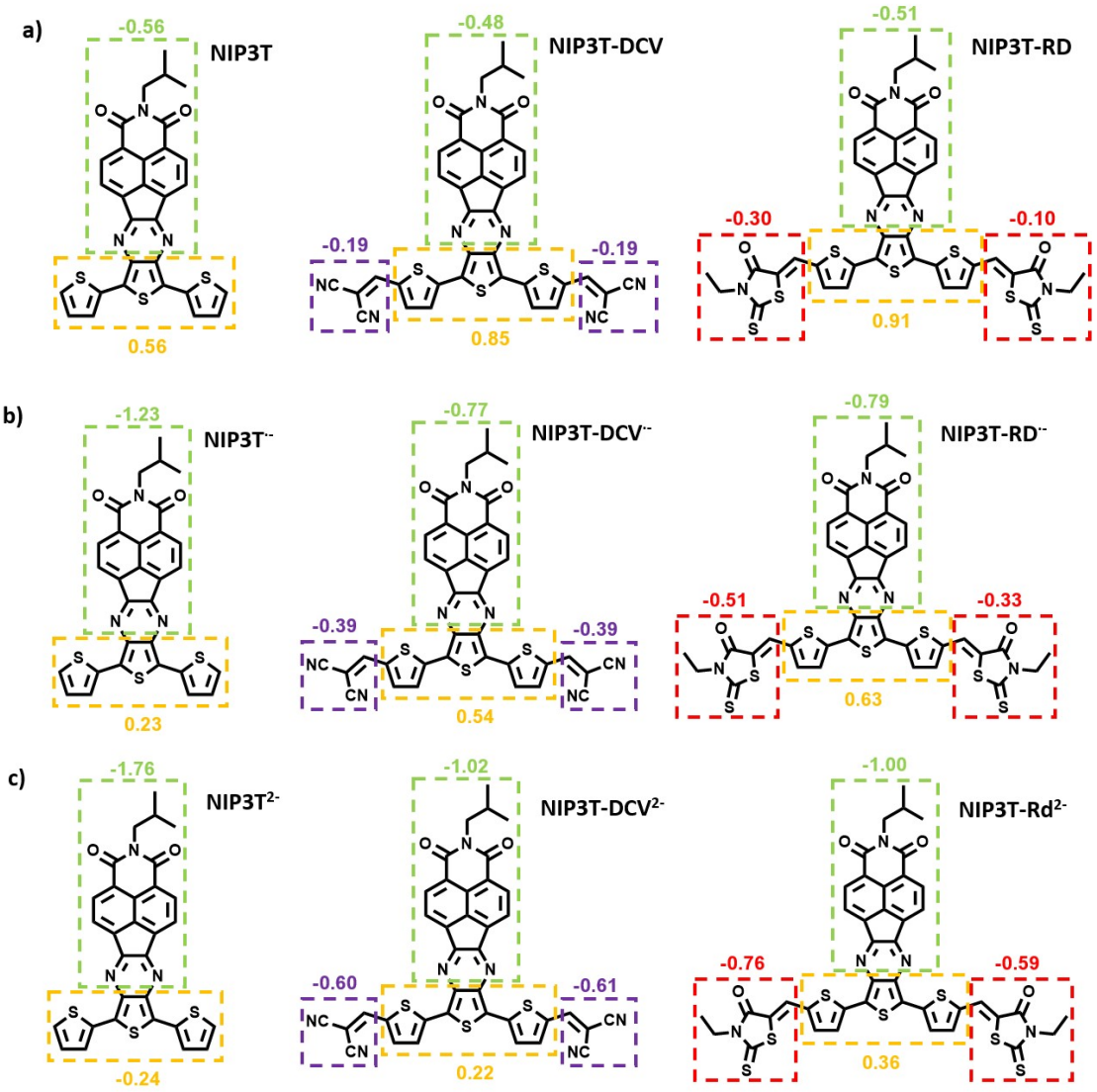

Figure S54. B3LYP/6-31G**-charge distributions for **NIP3T**, **NIP3T-DCV** and **NIP3T-Rd** as (a) neutral (b) anion and (c) dianion species.

7. References.

1. E. A. Weiss, M. J. Tauber, M. A. Ratner and M. R. Wasielewski, *Journal of the American Chemical Society*, 2005, **127**, 6052-6061.
2. A. P. Zoombelt, J. Gilot, M. M. Wienk and R. A. J. Janssen, *Chemistry of Materials*, 2009, **21**, 1663-1669.
3. M. J. Alonso-Navarro, A. Harbuzaru, P. de Echegaray, I. Arrechea-Marcos, A. Harillo-Baños, A. de la Peña, M. M. Ramos, J. T. López Navarrete, M. Campoy-Quiles, R. Ponce Ortiz and J. L. Segura, *Journal of Materials Chemistry C*, 2020, **8**, 15277-15289.
4. C. Lee, W. Yang and R. G. Parr, *Physical Review B*, 1988, **37**, 785-789.
5. A. D. Becke, *The Journal of Chemical Physics*, 1993, **98**, 5648-5652.
6. A. D. Becke, *The Journal of Chemical Physics*, 1993, **98**, 1372-1377.

7. P. C. Hariharan and J. A. Pople, *Theoretica chimica acta*, 1973, **28**, 213-222.
8. W. J. Hehre and W. A. Lathan, *The Journal of Chemical Physics*, 1972, **56**, 5255-5257.
9. G. W. S. M. J. T. Frisch, H. B.; Scuseria, G. E.; Robb, M. A.; Cheeseman, J. R.; Scalmani, G.; Barone, V.; Petersson, G. A.; Nakatsuji, H.; Li, X.; Caricato, M.; Marenich, A. V.; Bloino, J.; Janesko, B. G.; Gomperts, R.; Mennucci, B.; Hratchian, H. P.; Ortiz, J. V.; Izmaylov, A. F.; Sonnenberg, J. L.; Williams-Young, D.; Ding, F.; Lipparini, F.; Egidi, F.; Goings, J.; Peng, B.; Petrone, A.; Henderson, T.; Ranasinghe, D.; Zakrzewski, V. G.; Gao, J.; Rega, N.; Zheng, G.; Liang, W.; Hada, M.; Ehara, M.; Toyota, K.; Fukuda, R.; Hasegawa, J.; Ishida, M.; Nakajima, T.; Honda, Y.; Kitao, O.; Nakai, H.; Vreven, T.; Throssell, K.; Montgomery, J. A., Jr.; Peralta, J. E.; Ogliaro, F.; Bearpark, M. J.; Heyd, J. J.; Brothers, E. N.; Kudin, K. N.; Staroverov, V. N.; Keith, T. A.; Kobayashi, R.; Normand, J.; Raghavachari, K.; Rendell, A. P.; Burant, J. C.; Iyengar, S. S.; Tomasi, J.; Cossi, M.; Millam, J. M.; Klene, M.; Adamo, C.; Cammi, R.; Ochterski, J. W.; Martin, R. L.; Morokuma, K.; Farkas, O.; Foresman, J. B.; Fox, D. J. Gaussian, Inc., Wallingford CT., 2016.